

Machine learning analysis of the bleomycin-mouse model reveals spatial and temporal pulmonary inflammatory fingerprint

Natalie Bordag¹, Valentina Biasin^{1,2}, Diana Schnoegl¹, Francesco Valzano¹, Katharina Jandl^{1,3}, Bence M. Nagy¹, Neha Sharma^{1,4}, Malgorzata Wygrecka⁵, Grazyna Kwapiszewska^{1,3}, Leigh M. Marsh^{1*}

Affiliations

¹Ludwig Boltzmann Institute for Lung Vascular Research, Graz, Austria.

²Division of Endocrinology and Diabetology, Department of Internal Medicine, Medical University of Graz, Graz.

³Otto Loewi Research Center, Medical University of Graz, Graz, Austria.

⁴Division of Pulmonology, Department of Internal Medicine, Medical University of Graz, Graz, Austria.

⁵Department of Biochemistry, Universities of Giessen and Marburg Lung Center, Giessen, Germany. Member of German Center for Lung Research.

*to whom correspondence should be addressed:

Dr. Leigh Marsh

Leader of the Translational Platform

Ludwig Boltzmann Institute Lung Vascular Research

Center for Medical Research

Neue Stiftingtalstraße 6/VI

8010 Graz, AUSTRIA

Leigh.Marsh@lvr.lbg.ac.at

Impact statement

Unbiased immunophenotyping and data modelling exposes the dynamic shifts in immune cell composition, marking the transition from innate to adaptive immunity during bleomycin induced pulmonary fibrosis.

32 **Abstract**

33 The bleomycin mouse model is the most extensively used animal model to study pulmonary fibrosis.
34 Despite this, the inflammatory cell kinetics and cell compartmentalisation is still incompletely
35 understood. Here we simultaneously analysed 16 inflammatory cell populations in 303 samples and
36 applied advanced data modelling to conclusively detail these kinetics.

37 Three days post-bleomycin, the inflammatory profile was typified by acute innate inflammation,
38 pronounced neutrophilia and loss of alveolar macrophages. After 14 days, rapid responders were
39 increasingly replaced by the adaptive immune system and monocyte-derived alveolar macrophages,
40 which progressed till 21 days. Multi-colour imaging revealed the spatial-temporal cell distribution and
41 the close association of T-cells with fibrotic lung tissue at later time-points.

42 Unbiased immunophenotyping and data modelling exposed the dynamic shifts in immune cell
43 composition distinct for each phase of fibrosis process and defined the transition from innate to adaptive
44 immunity marking initial lung parenchyma remodelling.

45

46 **Keywords**

47 Bleomycin, mouse, inflammatory cells, machine learning, pulmonary fibrosis

48

49 **Abbreviations**

50 BALF, bronchoalveolar lavage fluid; BH, Benjamini-Hochberg; FCM, flow cytometry; IPF,
51 idiopathic pulmonary fibrosis; LOG_{x+1} , logarithm to the basis 10 of (x+1); ML, maximum likelihood;
52 MVA, multivariate analysis; NLME, non-linear mixed models; OPLS-DA, orthogonal projections to
53 latent structures discriminant analysis; PCA, principal component analysis; PF, pulmonary fibrosis;
54 UMAP, Uniform Manifold Approximation and Projection; UVA, univariate analysis; 4RT, fourth
55 root.

56 **Introduction**

57 Animal models of human disease are an invaluable tool to decipher disease relevant pathomechanisms,
58 to discover therapeutic targets and to drive translation into clinical practice. To date, the mouse
59 bleomycin-induced lung injury model is the most frequently used animal model to investigate
60 pulmonary fibrosis (B Moore et al., 2013; Della Latta et al., 2015; Tashiro et al., 2017). Similar to the
61 human situation, in mice bleomycin exposure is characterized by epithelial damage, inflammatory cell
62 infiltration, and expansion of fibroblasts and myofibroblasts as well as ECM deposition (Biasin et al.,
63 2020, 2017; El Agha et al., 2017; Tashiro et al., 2017; Xie et al., 2018). Although, the bleomycin model
64 does not completely recapitulate human idiopathic pulmonary fibrosis (IPF), it still remains the most
65 common and important animal model to study this disease.

66 IPF is a severe, rapidly progressing interstitial lung disease with high mortality rates and short median
67 survival of 1.5 - 4 years (Marshall et al., 2018; Wuyts et al., 2013). IPF is characterized by extensive
68 lung tissue scarring, limited inflammation and extracellular matrix remodelling (Meltzer and Noble,
69 2008). Current treatment options slow the loss of lung function, but are unable to halt or reverse disease
70 progression (Maher and Streck, 2019). Accordingly, there is an urgent unmet clinical need for novel
71 therapies for IPF patients. To date the aetiology and pathogenesis of IPF is still insufficiently
72 understood; however, the role of inflammation remains undeniable yet controversial. The older concept
73 that IPF is an inflammatory driven process has been gradually replaced by the theory of recurrent injury
74 and aberrant repair (Selman et al., 2001; Selman and Pardo, 2002; Wuyts et al., 2013). However,
75 multiple inflammatory cells have been implicated in disease pathogenesis, including macrophages
76 (Misharin et al., 2017; Reyfman et al., 2019) and T cells (Todd et al., 2013), which are connected with
77 poorer prognosis (Balestro et al., 2016).

78 In the bleomycin model, the early phase post bleomycin administration is characterised by acute lung
79 injury and inflammation, which is observed to last between 1-7 days (Peng et al., 2013). This
80 inflammatory phase is followed by active fibrosis, between 7-14 days and late fibrosis between, 21-28
81 days (Della Latta et al., 2015; Izbicki et al., 2002; Peng et al., 2013; Tashiro et al., 2017). As most
82 studies have only analysed specific cell populations or time points, a comprehensive description of the
83 inflammatory cell kinetics is still missing. For the detection and quantification of inflammatory cells,
84 flow cytometry (FCM) is the method of choice. FCM is able to differentiate and quantify immune cell
85 populations in unprecedented detail, not only from the circulation but also from disease relevant tissue
86 (Marsh et al., 2018; Misharin et al., 2017; Tighe et al., 2019a). In contrast to traditional
87 immunofluorescent staining, which generally use 1-3 markers for cell identification, flow cytometers
88 applies multiple markers to simultaneously quantify numerous cell populations at a single cell
89 resolution. Thus, FCM generates large quantities of complex data, where the analysis, visualization and

90 interpretation of which requires sophisticated analysis techniques, such as computational flow
91 cytometry (Saeys et al., 2016).

92 In order to conclusively detail the inflammatory cell kinetics in the bleomycin model, we here
93 assembled historical FCM data from 15 different experiments and applied advanced data modelling,
94 including univariate, multivariate and machine learning methods. We show how the combination of
95 advanced data modelling and in-depth immune profiling can detail the dramatic changes in the
96 inflammatory landscape in this model and also serves as a reference point.

97 Results

98 Pre-processing of flow cytometric data substantially improves statistical analysis performance

99 Intra-tracheal administration of bleomycin in mice, results in a time-dependent development of fibrosis
 100 (Figure 1AB). To comprehensively describe the inflammatory cell kinetics following bleomycin
 101 treatment, we assembled and conjointly analysed historical FCM data from 15 independent
 102 experiments, this resulted in 159 BALF and 144 lung tissue samples (Supplementary Table S1). Using
 103 standard gating strategies, a total of 16 cell populations covering the main myeloid and lymphoid cell
 104 types (Table 1) were identified (Figure 1C). The aggregation of historical experiments inherently led to
 105 an unbalanced experimental design (Supplementary Table S1), which was handled by robust statistical
 106 methods^[Box 1].

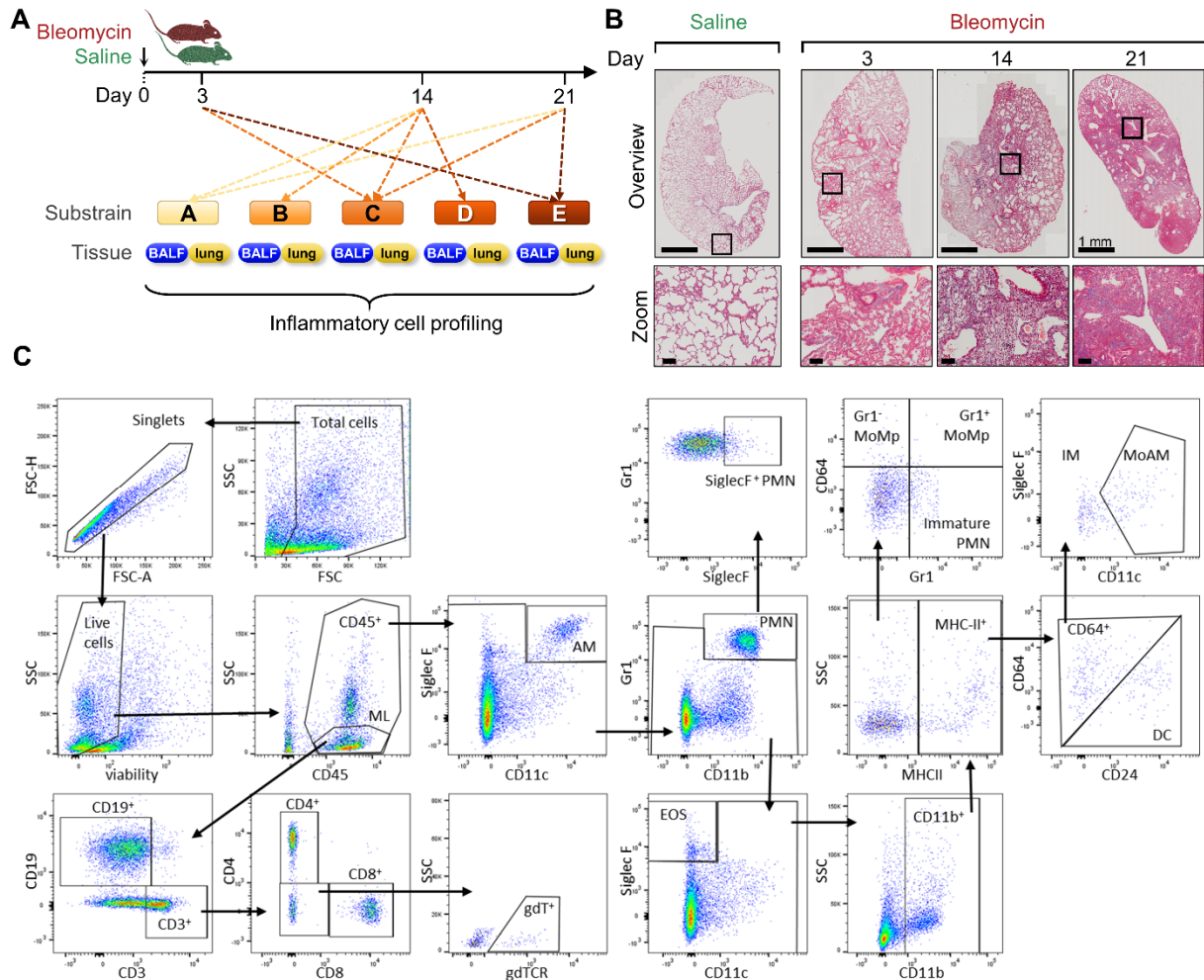
107 **Table 1. Inflammatory cell identification and corresponding markers.**

| Panel | Cell type | Abbrievation | Cell population | Panel I | | | | | | | Panel II | | | | | | | |
|----------|--------------|---------------------------|------------------------------------|---------|------|---------|-------|------|------|------|----------|-------|-----|-----|-----|------|-------|---|
| | | | | SSC | CD45 | SiglecF | CD11c | Gr-1 | CD64 | CD24 | MHC-II | CD11b | CD3 | CD4 | CD8 | CD19 | gdTCR | |
| | Cell count | | CD45 ⁺ live cell | | + | | | | | | | | | | | | | |
| Myeloid | Macrophages | AM | Alveolar macrophages | hi | + | + | + | | + | | +/- | | | | | | | |
| | | MoAM | Monocyte derived macrophages | | + | lo | + | | + | - | + | +/- | | | | | | |
| | | IM | Interstitial macrophages | | + | - | - | | + | - | + | +/- | | | | | | |
| | DCs | DC | CD11b ⁺ Dendritic cells | | + | | | - | - | + | + | + | | | | | | |
| | Monocytes | Gr1 ⁺ MoMp | Inflammatory monocytes | | + | | | | + | + | | - | + | | | | | |
| | | Gr1 ⁻ MoMp | Constitutive monocytes | | + | | | | - | | | - | + | | | | | |
| | Granulocytes | EOS | Eosinophils | | hi | + | + | - | | | | | + | | | | | |
| | | PMN | Mature neutrophils | | hi | + | +/- | - | + | | | | + | | | | | |
| | | SiglecF ⁺ PMN | SiglecF ⁺ neutrophils | | hi | + | + | - | + | | | | + | | | | | |
| | | Immature PMN | Immature neutrophils | | hi | + | | - | + | | | | - | + | | | | |
| Lymphoid | B cells | CD19 ⁺ B cells | B cells | | lo | + | | | | | | | - | | | | + | |
| | T cells | CD3 ⁺ T cells | T cells | | lo | + | | | | | | | | + | | | | - |
| | | CD4 ⁺ T cells | T helper cells | | lo | + | | | | | | | | + | + | - | - | |
| | | CD8 ⁺ T cells | Cytotoxic T cells | | lo | + | | | | | | | | + | - | + | - | |
| | | $\gamma\delta$ T cells | $\gamma\delta$ T cells | | lo | + | | | | | | | | + | + | - | - | + |

108

109

110

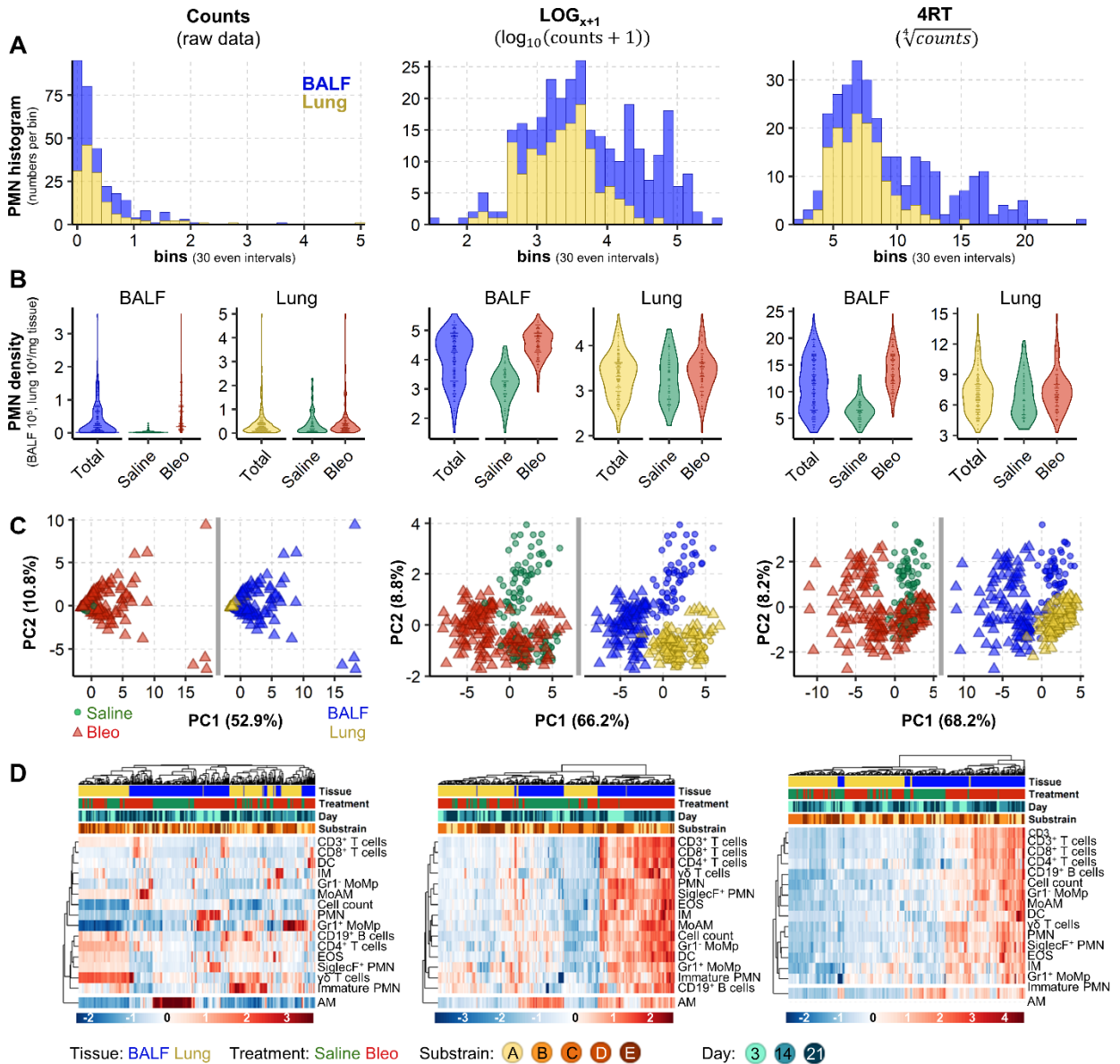


111

112 **Fig. 1.** Overview of study design, pathological changes and gating strategy. (A) Historical flow cytometry data from the
 113 bleomycin mouse model were pooled and collectively analysed. Samples were collected 3, 14, or 21 days post
 114 bleomycin or saline administration from the compartments BALF (159 samples) and lung tissue (144 samples). Five
 115 different C57BL/6 substrains were included. (B) Representative Masson's trichrome staining of lung sections, showing
 116 pathologic alterations in the bleomycin model. Zoomed images exemplify the increasing fibrosis accumulation from
 117 day 3 to 21 after bleomycin challenge, scale bar represents 100 μ m. (C) Representative flow cytometry gating strategy.
 118 Abbreviations see Table 1.

119 In both tissues the distribution of all 16 analysed cell populations was significantly non-normal with a
 120 positive skew^[Box 1] (Fig. 2A, Supplementary Fig. S1 and Supplementary Data 1). To improve
 121 distribution we trialled several common transformations; square root, reciprocal, Freeman Tukey, logit,
 122 LOG, LOG_{x+1} and 4RT. Only LOG, LOG_{x+1} and 4RT improved data distribution ($p_{BH}>0.05$,
 123 Supplementary Data 1). As both LOG and LOG_{x+1} gave virtually equivalent results, but as LOG_{x+1} has
 124 additionally the advantage of not introducing missing values for zero value counts, consequent analysis
 125 was performed with only LOG_{x+1} and 4RT (Fig. 2AB).

126



127

128

129

130

131

132

133

134

Fig. 2. Data transformation improves data distribution and analytical power. Analysis of cell count data (untransformed) or following transformation using LOG_{x+1} or 4RT (fourth root) using 159 BALF and 144 lung samples. Cell counts in BALF are 10^5 and in lung $10^4/\text{mg}$ tissue. Examples of data distribution of neutrophils (PMN) as one representative population in BALF and lung samples by (A) Histograms and (B) Violin plots, total represents combined saline and bleomycin samples. (C) PCA scores plots with each point representing the inflammatory cell profile (16 populations) in one sample, plots are coloured to highlight different experimental conditions. In B and C, dots represent single sample values. (D) Heatmaps with hierarchical clustering of all 16 analysed cell populations.

135

Bleomycin drives strong changes in the inflammatory profile

136

137

138

139

140

To identify global changes in the inflammatory cell profile, we first applied unsupervised principal component analysis (PCA). This method reduces dimensionality by creating new variables, which successively maximize variance and thereby aids data interpretability. Without data transformation, the scores plot was dominated by single sample differences, which obscured any experimental effects (Fig. 2C, left panel). After transformation pronounced differences in the inflammatory profile were revealed

141 (Fig. 2C). Both LOG_{x+1} and 4RT substantially improved the performance of the hierarchical clustering
142 (HC), yielding clearer clustering and heatmap results (Fig. 2D). The highest influence on the
143 inflammatory landscape was caused by the tissue compartment (BALF or lung), causing samples to
144 separate along the first principal component (PC1). The second highest difference was caused by
145 bleomycin, separating samples in the BALF along the second principal component (PC2; Fig. 2C,
146 middle and right panels). Similarly, HC was first driven by the tissue compartment, followed by some
147 weaker subclustering due to bleomycin treatment. The majority of cell populations increased after
148 bleomycin exposure, while alveolar macrophages (AlvMp) decreased (Fig. 2D). We next utilised
149 macroPCA, a robust PCA method able to handle and identify all possible types of data
150 contaminations^[Box 1], including strong single value or sample outliers (Hubert et al., 2019). MacroPCA
151 results were in good agreement with PCA (Supplementary Fig. S2A), which confirmed that this dataset
152 is free of severe outliers allowing the use of a wide variety of statistical methods (Rousseeuw and
153 Hubert, 2018).

154

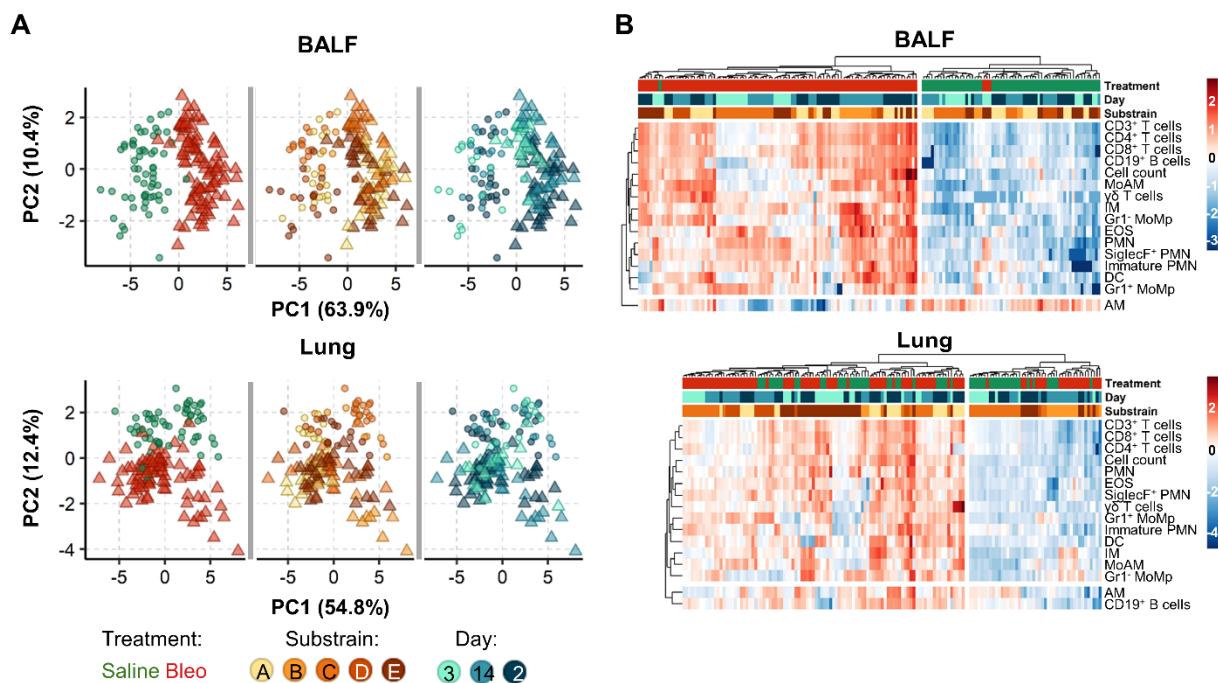
Box 1 | Glossary of analysis terms

| | |
|----------------------------|--|
| robustness | is a measure for how easily outlier values distort results, e.g. <ul style="list-style-type: none">• average: not robust, a single strong outlier deforms results severely• median: very robust, good results even with almost half of all values being strong outliers |
| unbalanced | describes unequal group sizes or missing values, methods assuming balanced groups will have misleading results |
| positive skew | asymmetric distribution of data with more large than small values, common in flow cytometry and many other biological measures (often because zero is the minimum, while there is no fixed maximum) |
| data preprocessing | preprocessing normalises data by changing all values according to one or several defined mathematical equations and can be a prerequisite for specific statistical methods Centring and scaling <ul style="list-style-type: none">• cell count differences are not per se reflective of their biological importance• centring and scaling minimizes the stark differences of cell numbers between the cell populations allowing comparisons of fold changes• are vital for multivariate statistical methods, otherwise results will be dominated by cells with highest counts/highest noise Transformation <ul style="list-style-type: none">• improves data distribution allowing use of more powerful statistical methods (Keene, 1995; van den Berg et al., 2006) all types of preprocessing can be combined with each other |
| centring | subtraction of a constant from every value (e.g. the average of each cell population) |
| scaling | every value is divided by a constant (e.g. the standard deviation, SD) |
| transformation | convert each data point by a specific, often nonlinear, but defined mathematical function (e.g. \log_{10}) |
| data contaminations | denotes all kinds of problematic values in the data, such as sample outliers, single value outliers or missing values |
| outlier | a value so different from the rest, that it could be for example an analytical error |

155

156 As the strong compartment effect could mask weaker drivers that alter the inflammatory landscape, we
 157 analysed BALF and lung samples separately (Fig. 3). In the BALF, bleomycin exposure completely
 158 altered the inflammatory landscape, separating samples along PC1 (explaining 63.9 % of the variation
 159 in the dataset). However, the bleomycin effect only accounted for 12.4 % of the variation in the lung,
 160 separating on PC2 (Supplementary Fig. S2A). Again, macroPCA gave similar results in the analysis of
 161 the separate compartments (Supplementary Fig. S2B), reconfirming absence of critical outliers.
 162 Analogous to the PCA findings, HC showed a strong clustering after bleomycin exposure in BALF,
 163 which was less clear in lung. The influence of day post-treatment and substrain (individual C57BL/6J
 164 lines) on cell population changes was less distinct, with only some indication towards a possible sub-
 165 clustering due to these factors (Fig. 3B).

166



167

168 **Fig. 3.** Bleomycin induces stronger changes in the inflammatory profile in the BALF than the lung. The contribution of
 169 different biological factors to the inflammatory cell profile as determined by (A) PCA scores plots are coloured to
 170 highlight different experimental conditions, and (B) Heatmaps with hierarchical clustering. To aid interpretation
 171 heatmaps are split into two main clusters based on dendrogram distances. Colours and shapes represent tissue,
 172 treatment (Saline, Bleo), mouse substrain and day post treatment. Cell counts from 16 populations in 159 BALF and
 173 144 lung samples were LOG_{x+1} transformed prior to clustering.

174 Modelling of inflammatory cell kinetics with univariate statistical analysis

175 In order to examine in depth, the potential influence of other experimental factors and to simultaneously
 176 control for the unbalanced design arising from the use of historical data, we applied non-linear mixed
 177 models (NLME, Supplementary Fig. 3). As the multivariate analysis showed a strong bleomycin effect,
 178 the fixed factor^[Box 2] *Treatment* {Saline,Bleo} was included in all models^[Box 2]. Other fixed factors

179 included *Day* {3,14,21} and *Substrain* {A,B,C,D,E}. The addition of each factor, either alone or
180 together and with or without their interaction with *Treatment*, notably improved the fit^[Box 2] of all simple
181 models, increasing the goodness of fit and reducing AIC (Supplementary Fig. S3). Thus, both the *Day*
182 post bleomycin exposure and *Substrain* significantly influenced the cellular landscape.

183

Box 2 | Glossary of model terms

| | |
|------------------------|---|
| model | a mathematical equation to describing the relationship of measured data to biological factors <ul style="list-style-type: none">• imagine you assume that the weight increases with height, than the biological factor is body height, the measured data is weight and a linear model would have the equation: $weight = a \cdot height + b$• parameters are a and b, a – inclination (steepness of the line), b – intercept (<i>weight</i> at <i>height</i>=0) |
| fitting | finding the best parameter values in the mathematical equation of the model, parameters are optimized to bring the line/curve of the model nearest to the data, often assessed by the residuals |
| fixed factor | also called between-subject effect, a biological factor which (possibly) affects the outcome <ul style="list-style-type: none">• height is a fixed factor in the example, gender would be another possible fixed factor |
| interaction | the impact of one biological factor depends on the occurrence of another biological factor <ul style="list-style-type: none">• imagine to include also gender and genetics as biological factors, the effect that males are roughly 0.13 m taller than females is much smaller in achondroplasia which results in short stature |
| random factor | also called within-subject effect, a factor which (possibly) affects baseline level such as repeated measures from the same source or working in experimental batches <ul style="list-style-type: none">• in linear model example that is to measure the height/weight yearly during adolescence while smaller |
| simple/mixed | simple models have no random factor, mixed models have a random factor |
| residuals | difference between fitted value and measured value <ul style="list-style-type: none">• in linear model example that is the distance from the measured value to the line |
| fitted value | the value suggested by the equation for the specific value of the biological factor <ul style="list-style-type: none">• in linear model example that would at a given height the weight on the line |
| predicted value | similar to fitted values the predicted value is suggested by the model equation, but for formerly unknown points (unknown during model fitting or not measured at all) <ul style="list-style-type: none">• imagine the linear model was based on heights from 1 – 1.5 m and you want to predict the weight for 1.7 m |
| overfitting | the model contains more parameters than possible from the data, fails to predict new data correctly <ul style="list-style-type: none">• in the example adding irrelevant factors (e.g. birthdates, house numbers, number of earrings, ...) can produce perfect fits but fail to predict new values |

184

185 As each independent experiment could have similarities, the experimental ID was then included as a
186 random factor ($\sim 1 | Exp_ID$). These mixed models significantly outperformed the aforementioned simple
187 models. Finally, complex mixed models (combining the mixed models with the interactions of
188 *Treatment* with *Substrain* or *Day*) notably outperformed all simple models (with or without
189 interactions). The most complex mixed model [*Treatment+Day+Substrain+Treatment:Substrain+*
190 *Treatment:Day, ~1|Exp_ID*] outperformed all other models, although more prominently in BALF than
191 in lung (Supplementary Fig. S3A).

192 As complex models risk overfitting, especially in light of the unbalanced design, we then investigated
193 model simplification. We first tested whether it was possible to create one control group of all saline

194 animals. In all mixed and complex models (i.e. with random factor *Exp_ID*) only 4 of the over 10000
195 investigated pairwise comparisons of a saline subgroup with another saline subgroup had a $p_{BH} < 0.01$ in
196 any of the 16 cell types. This means saline treated animals were sufficiently similar to be combined into
197 one control group. Consequently, *Treatment* and *Day* can be then merged into one fixed factor with
198 four groups: Saline (all days) and bleomycin after days 3, 14, and 21, which was termed *SalineDay*
199 $\{\text{Saline}, 3, 14, 21\}$, generating the simplified model [*SalineDay+Substrain*] and the simplified mixed
200 model [*SalineDay+Substrain~I|Exp_ID*]. The performance of the simplified mixed model was slightly
201 lower than in the most complex mixed model, but well within the range of the other top performing
202 mixed models (Supplementary Fig. S3B).

203 To compare the models in more detail we also directly compared the fitted values^[Box 2] of the simplified
204 mixed model with the most complex mixed model. The fitted values from both models strongly
205 correlated (Pearson correlation $R^2 > 0.96$, Supplementary Fig. S3B). This underlines the validity of
206 model simplification and that no unexpected or systematic skew was introduced. As the simplified
207 mixed model [*SalineDay+Substrain~I|Exp_ID*] also gives more easily interpretable results and has a
208 lower risk of overfitting^[Box 2], it was chosen to examine the inflammatory cell kinetics underlying
209 bleomycin mouse model.

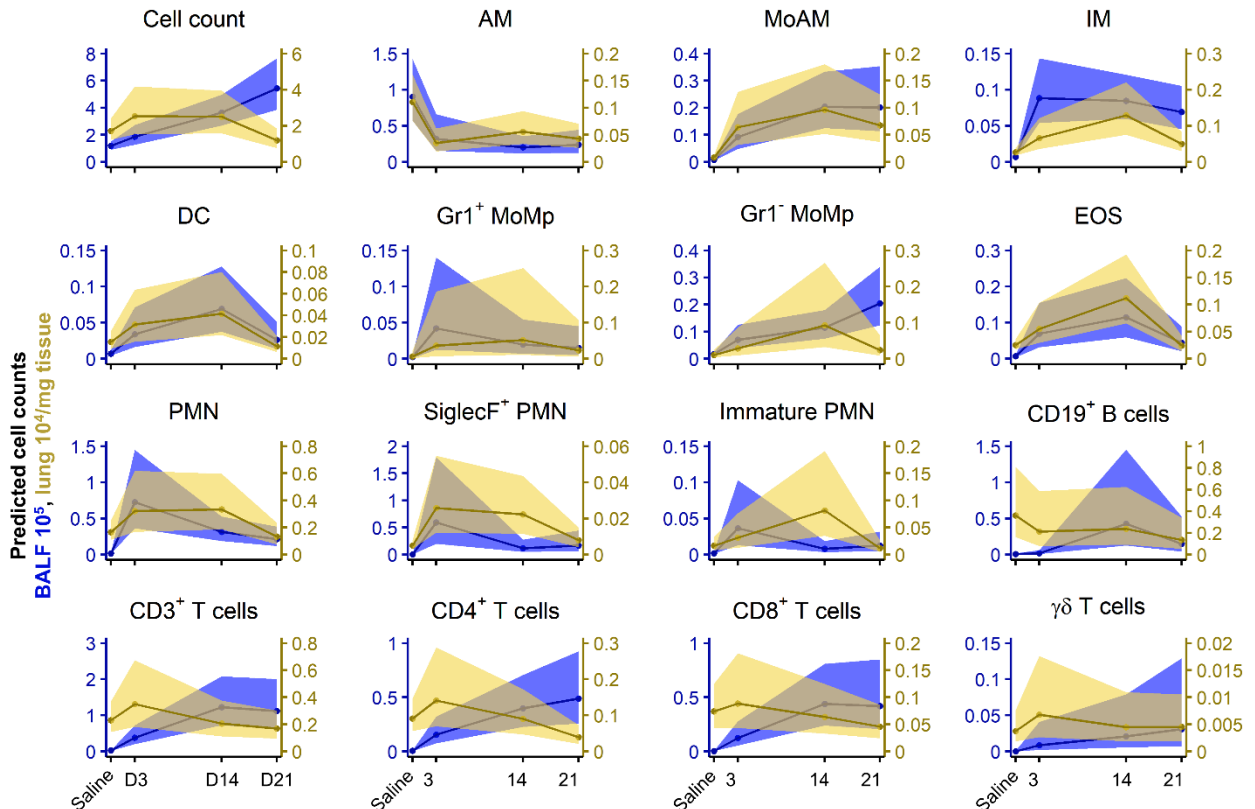
210 This model was then applied to explore how individual substrains may influence the kinetics of different
211 inflammatory cells. All mice included in this study are on the C57BL/6 background, however were
212 obtained from different sources e.g. commercial sources (C57BL/6J, substrain A), or are the wild-type
213 littermates from in-house breedings (substrains B-E). Although some lines were inbred for up to 15
214 generations, all mouse lines produced similar inflammatory responses in both lung compartments,
215 differing only in magnitude (Supplementary Fig. S4). This consistency allows to read out the
216 compartmental kinetics of each cell population after bleomycin treatment for all substrains combined.

217 **Inflammatory cell kinetics after bleomycin-induced lung injury are robust and reproducible**

218 Analysis of the inflammatory response in the BALF, identified a non-resolving inflammatory response,
219 with the total number of inflammatory cells continuing to increase over the investigated time course of
220 21 days. In the lung tissue, inflammation was characterized by an immediate increase at day 3,
221 stagnating to day 14 and mostly resolved 21 days post bleomycin exposure (Fig. 4). This suggests that
222 the inflammatory response is persistent, yet compartment dependent.

223 Early inflammatory changes were mostly dominated by the innate immune system, including both
224 immature and mature neutrophils, monocyte-derived alveolar and interstitial macrophages. In contrast
225 we observed a concomitant decrease in alveolar macrophages. Interestingly, the (inverted) trajectories
226 of alveolar macrophages were comparable to the rise in monocyte-derived macrophages, suggesting a
227 functional replacement by the latter and supports observations in earlier studies (Misharin et al., 2017).
228 Following the rapid increase in the first line responders, neutrophils, their numbers later stagnated or

229 gradually decreased, and even returned to baseline levels in the lung tissue. We also identified a time-
 230 dependent increase in SiglecF⁺ neutrophils following bleomycin application. These cells have recently
 231 been described to be important for cancer progression (Engblom et al., 2017). Similarly, eosinophils
 232 and dendritic cells (EOS, DC) exhibited a bell-shape response curve. In contrast monocyte populations
 233 (both constitutive and inflammatory) exhibited a slower, but consistent, step wise increase over time,
 234 which could be attributed to their contribution to both the innate and adaptive immunity and their role
 235 in tissue repair.

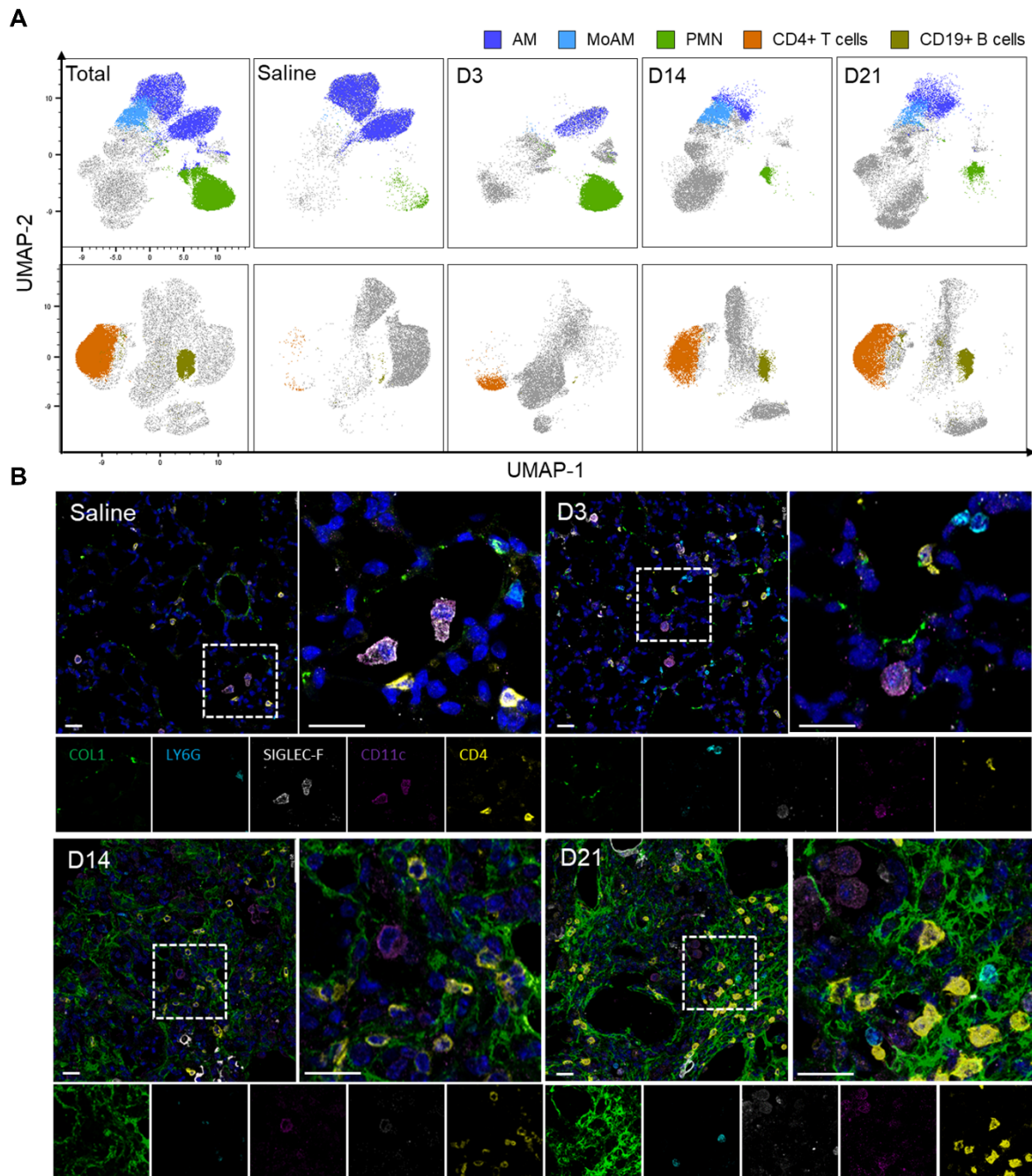


236
 237 **Fig. 4.** Non-linear mixed models reveal complex immune cell dynamics occurring in the lung following bleomycin induced
 238 lung injury. Plot of back transformed, fitted cell counts (line represents mean \pm 95 % confidence intervals) using the
 239 simplified mixed model [*SalineDay+Substrain~1|Exp_ID*] of LOG_{x+1} transformed cell counts for BALF (counts \cdot 10⁵)
 240 and lung tissue (counts \cdot 10⁴/mg tissue). Animal numbers were in BALF in total n = 159 (Saline 60; 3d 23; 14d 39; 21d
 241 37) and in lung in total n = 144 (Saline 56; 3d 23; 14d 32; 21d 33).

242 At later time points, inflammation was dominated by immune cells from adaptive immunity, with a
 243 clear preference to the alveolar compartment. While CD3⁺ T lymphocytes (CD4⁺ and CD8⁺ T cells,
 244 respectively) had a steep, yet non-resolving, rise early in the inflammatory response, the CD19⁺ B cells
 245 peaked at 14 days post bleomycin challenge. Interestingly, at the latest time point, 21 days, B cells
 246 numbers still continued to rise, implicating their involvement at later stages in this model (Fig. 4A).

247 Taken together, the multiple inflammatory cell populations show dynamic and distinct inflammatory
 248 kinetics with clear compartment preferences. With time the involved immune cells shifted from the

249 innate to the adaptive immune system, with the BAL being more prominently affected than the lung
250 tissue. After 21 days the inflammatory profile was still chronically altered.



251

252

253

254

255

256

257

Fig. 5. Temporal and spatial localization of inflammatory cell kinetics in BALF and lung tissue. (A) Uniform Manifold Approximation and Projection (UMAP) plots of concatenated CD45⁺ populations (min 3 independent samples with max 10⁶ CD45⁺ cells per sample) with overlaid manually gated populations in BALF. (B) Spatial localisation of alveolar macrophages (CD11c⁺/SiglecF⁺), neutrophils (LY6G⁺), and CD4⁺ T cells during the time course of bleomycin challenge. Nuclei are stained with DAPI (dark blue). Representative pictures of three independent mice at each time point. D3, D14 and D21, represent days 3, 14 and 21 post-bleomycin treatment, respectively.

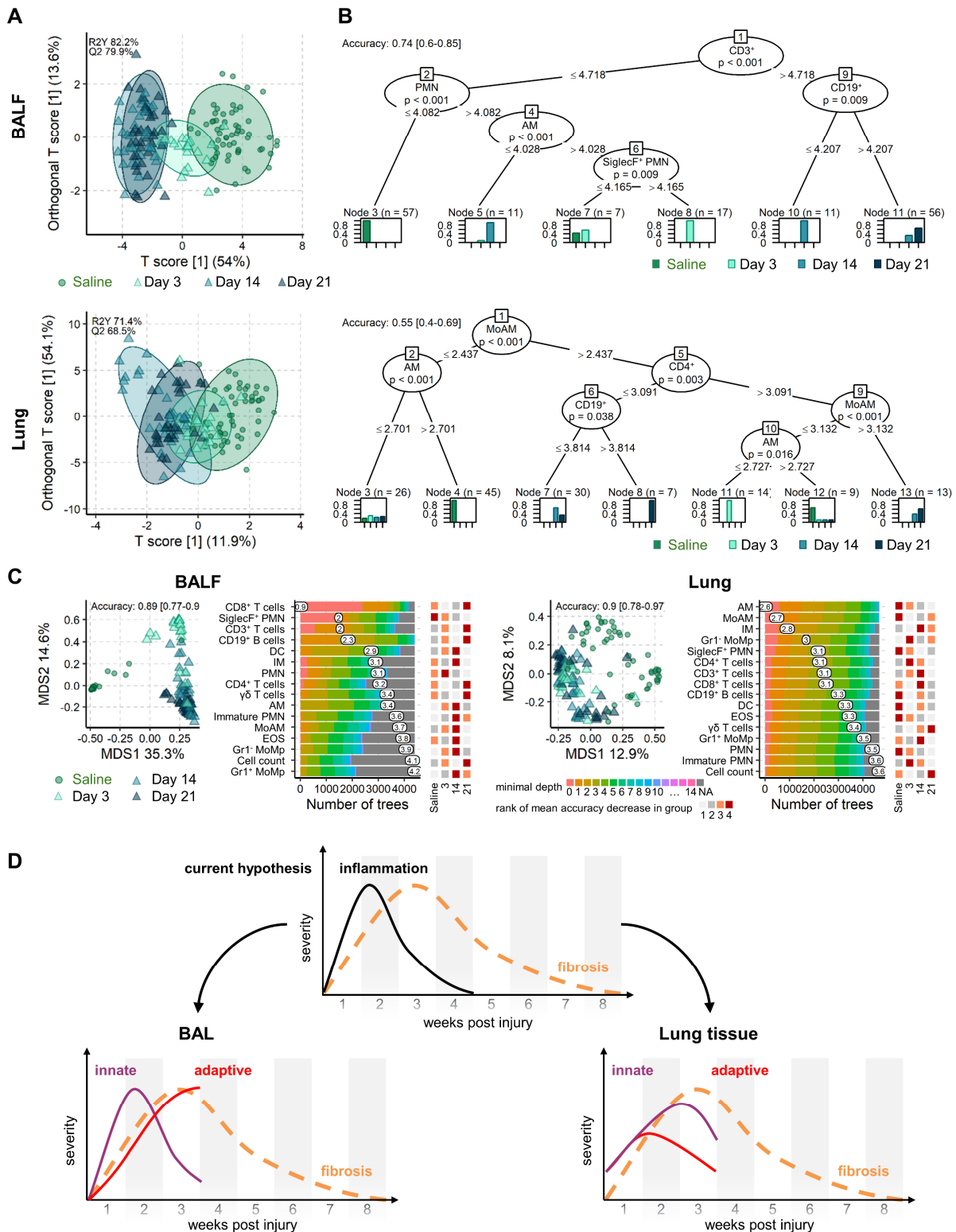
258 Based on these results we went back to our FCM data and visualised the kinetics of the most
259 dynamically altered populations via computational FCM (Fig. 4B). As predicted in our modelling data
260 AM populations strongly decreased after bleomycin exposure, while the innate PMNs vastly expanded
261 after 3 days. Adaptive immune cells such as CD4⁺ T cells, CD8⁺ T cells and CD19⁺ B cells expanded
262 more at later time points and were virtually absent in saline treated mice (Fig. 5A). Visualisation using
263 multi-colour immunofluorescence revealed the co presence of CD11c⁺/SiglecF⁺ AM, CD4⁺ T cells and
264 Ly6G⁺ neutrophils in fibrotic lung tissue (Fig. 5B), the spatiotemporal presence of these cells point
265 toward close interplay between inflammatory components.

266 **The inflammatory cell landscape continually evolves following bleomycin exposure**

267 The combination of unsupervised multivariate methods and univariate NLME identified the kinetics of
268 each cell type with an early innate response followed later by adaptive immune response. However, the
269 question how the entire landscape differs between different timepoints or which cell types define each
270 stage is still open. In order to answer these questions, we applied three robust machine learning
271 approaches.

272 Our first approach, OPLS-DA separates the dataset into predictive and non-predictive components.
273 Predictive means the ability to discern between groups in the given classification factor, which was here
274 *SalineDay* {Saline,3,14,21}. The OPLS-DA model quality was thoroughly investigated by cross-
275 validation and permutations tests showing that in both compartments the models were highly significant
276 (Q²>50 %, p<0.001). Similar to our PCA results (Fig. 3), the inflammatory reaction was more
277 pronounced in the BALF than in the lung, as apparent from a clearer group separation, higher
278 percentages of variability in the predictive component and higher predictive ability (Q²; Fig. 6A). In
279 BALF, the inflammatory landscape at 14 and 21 days post bleomycin were very similar, but very
280 different from the saline controls, while the landscape at 3 days bridged these two poles.

281 We next investigated conditional inference trees and random forest models to infer which cell
282 populations were the driving factors behind the group differences. Conditional inference trees in the
283 BALF demonstrated that CD3⁺ T cells levels separated early (Saline, D3) and later timepoints (D14,
284 D21). Separating samples on low and high CD19⁺ B cells distinguishes between days 14 and 21,
285 respectively. On the other hand, low levels of PMN strongly predicts saline treated mice and the
286 combination of low AM and SiglecF⁺ PMN aiding the separation between saline, D3 and D14 (Fig.
287 6B). In the lung compartment, both innate cells (MoAM, AM) and adaptive (CD4⁺ T cells and CD19⁺
288 B cells) were needed to define the different groups. Saline mice were defined by low levels of MoAM
289 and high AM, while bleomycin treatment by high MoAM and CD4⁺ T cells. Similar to the BALF, day
290 21 was marked by high CD19⁺ levels, while D14 by was defined by lower B cell and MoAM levels
291 (Fig. 6B). A combination of low MoAM and low AM defined day 3.



292

293

294

295

296

297

298

299

Fig. 6. Exploration of inflammatory cell landscape differences with machine learning in BALF and lung tissue. (A) Scores plot of OPLS-DA models per compartment for the factor *SalineDay* {Saline,3,14,21} with 95 % confidence ellipses for each group. The predictive ability of the models Q^2 was calculated by 7-fold cross validation and 1000 permutation tests reconfirmed model significance with $p < 0.001$. (B) Conditional inference trees per compartment, showing cell types and cut-offs that define each group; saline, days 3, 14 and 21 post bleomycin treatment (*SalineDay*). Model accuracy was evaluated with a stratified split into 65 % trainings and 35 % test set. (C) MDS plot (left panel) of the proximity matrix of random forest models grown with 5000 trees. Model accuracy was evaluated with a stratified split

300 into 65 % trainings and 35 % test set. The distribution of the minimal depth is shown for each cell type according to
301 the number of trees, the mean of the minimal depth is shown (middle panel). The rank of the mean decrease in accuracy
302 within each group is shown for each cell population (right panel). Animal numbers in all models from A-C were in
303 BALF in total n = 159 (Saline 60; 3d 23; 14d 39; 21d 37) and in lung in total n = 144 (Saline 56; 3d 23; 14d 32; 21d
304 33). Models were based on LOG_{x+1} transformed cell counts for BALF (counts $\cdot 10^5$) and lung tissue (counts $\cdot 10^4/\text{mg}$
305 tissue). (D) Schematic, abstracted summary of all previous findings differentiating between the compartments BAL and
306 lung tissue.

307 Random forest models were then used to compare the ability of all cell populations to drive group
308 separation. In agreement with previous results, again group separation was clearer in BALF than in
309 lung, as demonstrated by multi-dimensional scaling plots of the random forest proximity matrix and
310 higher accuracy (Fig. 6C). In BALF especially the adaptive immune cells CD8^+ and CD3^+ T cells as
311 well as the innate SiglecF^+ PMN differed most, as became apparent from their low minimal depth.
312 Between the different groups high CD8^+ , CD3^+ and CD19^+ levels were most predictive for late
313 inflammation while low SiglecF^+ PMN levels were most predictive for the cellular landscape in saline
314 samples. The random forest suggests some fine but distinct differences between the global inflammatory
315 landscape 14 and 21 days after bleomycin exposure (Fig. 6C). Although both are highly inflamed
316 (OPLS-DA), higher levels of adaptive cells are rather predictive for day 21 (e.g. all T and B cells), while
317 higher levels of some innate cells are more predictive for day 14 than day 21 (e.g. DC, IM, immature
318 PMN, MoAM, EOS) or day 3 (PMN). In contrast, lung models were dominated by macrophage cell
319 populations differing most between the inflammatory stages, foremost the depletion of alveolar
320 macrophages. The random forest models underline that the inflammatory landscape differs notably
321 between lung and BALF.

322

323 Discussion

324 In this study, we have combined computation FCM, advanced data modelling and machine learning
325 approaches to conclusively define the inflammatory cell kinetics following bleomycin treatment in
326 mice. By combining the data from 15 independent experiments, we amassed very large sample numbers,
327 which were far in excess of those normally found in animal experiments. The aggregation of historical
328 samples inherently led to an unbalanced experimental design, which was handled by sophisticated,
329 robust statistical methods. By using pre-processing techniques such as data transformation, we could
330 substantially improve analysis power, which crucially contributed to clearer data interpretation.
331 Changes in the inflammatory profile was dissected using multivariate and univariate statistical methods
332 including non-linear mixed models. Only by applying these techniques in unison were we able to create
333 the most comprehensive picture of inflammatory cell trajectories to date and characterise the sustained
334 inflammation in the bleomycin model of pulmonary fibrosis.

335 FCM data is normally highly asymmetric i.e. it has many larger values but no values smaller than zero,
336 this non-normal distribution prevents the use of more powerful analysis methods. To re-establish
337 normality we trialled several transformations, but ultimately settled on LOG_{x+1} as it normalised the data
338 distribution, can be easier to interpret and also slightly improved the scedasticity compared to 4RT. Our
339 data modelling approach resulted in a very large sample size, which notably increased statistical power
340 and outweighed the potential drawbacks of added confounding variation from experimental runs or the
341 use of different substrains. Furthermore, when experimental covariance was accounted for as random
342 factor in NLME models, the inflammatory profiles in the BALF and lung tissue of all saline treated
343 animals, irrespective of experiment, were sufficiently similar to be combined into one large control
344 group. Secondly, the trajectories of inflammatory cell profiles were found to be consistent for all five
345 substrains, although their magnitudes slightly differed, which is important for experimental
346 reproducibility in light of using different knockout lines or mice sourced from different companies.

347 The application of unsupervised and supervised as well as multivariate and univariate, demonstrated
348 how the changes for most populations were more prominent in the BALF than in lung tissue, although
349 the majority of populations showed consistent trajectories in both compartments. In healthy mice, the
350 vast majority of cells in the BALF are alveolar macrophages, while in the lung tissue even at baseline
351 conditions, a highly heterogenous pool of inflammatory cells exists, including macrophages neutrophils,
352 T and B cells. Due to the higher sensitivity of the BALF to monitor inflammatory changes, we would
353 recommend this as the compartment of choice for the majority of cells in FCM analysis. Analysis of
354 the BALF has further advantages such as being easily accessible, without need for additional tissue
355 digestion steps.

356 Our comprehensive analysis of multiple inflammatory cell population at several time-points, describes
357 the kinetics not only during disease development but also when it is fully established. The initial

358 inflammatory phase after bleomycin exposure was dominated by early responder cell types from the
359 innate immune system of the myeloid lineage. Neutrophils constitute the first line defence of the
360 immune system and consequently show very acute kinetics, being rapidly recruited and also being the
361 first cell type to resolve, visible as pronounced decreases from day 3 to day 14 after the challenge. In
362 contrast, cells from adaptive immune system, such as B and T cells, increased much slower but continue
363 to expand even at 21 days. The worth of subtyping cell populations is apparent by the inverse kinetics
364 displayed within macrophages, which is only possible by using multicolour analysis. We could show
365 that while the numbers of alveolar macrophages (AlvMp) quickly decrease, monocyte derived
366 macrophages (MoAM) increase. These contrary trajectories would explain the early observation that
367 macrophage numbers were unchanged in this model (Izbicki et al., 2002), but the closer analysis of
368 macrophage subtypes revealed strong dependent changes, as shown by (Misharin et al., 2017, 2013)
369 and now reconfirmed by our results.

370 Increasingly macrophage heterogeneity has been suggested to play an important role in the pathogenesis
371 of lung fibrosis and have implications for therapeutic strategies. MoAM undergo marked transcriptional
372 changes during their differentiation in the injured lung tissue. These changes are not only associated
373 with a continuous down-regulation of genes typically expressed in monocytes and up-regulation of
374 genes expressed in alveolar macrophages but also with markedly elevated expression of
375 proinflammatory and profibrotic genes related to M1 and M2 phenotype. This unique transcriptomic
376 signature of MoAM provides an explanation how bleomycin-induced lung fibrosis is attenuated
377 following selective depletion of these cells (Joshi et al., 2020; McCubbrey et al., 2018; Misharin et al.,
378 2017). Interestingly, the existence of common profibrotic pathways in MoAM harvested from mice
379 during fibrosis development and profibrotic macrophages obtained from the lungs of IPF patients has
380 been reported (Aran et al., 2019; Misharin et al., 2017). All these observations strongly suggest that
381 selective targeting profibrotic macrophages, rather than the M1 or M2 phenotype, is more likely to be
382 of benefit in such a complex disease as IPF. The potential contribution of MoAM to the resolution of
383 lung fibrosis is still open and remains the subject of future studies. Recent data supports this hypothesis
384 (Cui et al., 2020). Hence, MoAM could represent very plastic cell population with distinct functions in
385 different phases of lung fibrogenesis.

386 Early and late fibrotic stages were characterized by increased numbers of T and B cells in the BALF,
387 while numbers in the lung tissue remained relatively stable, this reflects earlier reports describing the
388 presence of T cells in IPF lungs (Balestro et al., 2016; Todd et al., 2013). Here B cells are of particular
389 interest, as abnormal B cell aggregates have been described in IPF lungs (Marchal-Sommé et al., 2006)
390 and diverse circulating IgG autoantibodies were found in IPF plasma (Kurosu et al., 2008; Ogushi et
391 al., 2001; Taillé et al., 2011). Furthermore, individual auto-immunoglobulins were linked to severity
392 and/or poor prognosis of IPF (Kahloon et al., 2013; Ogushi et al., 2001) thus suggesting the causal role
393 of certain autoantigens in IPF. Accordingly, transcriptome-profiling of lung tissue derived from

394 pirfenidone-treated patients revealed downregulation of B cell related genes (Kwapiszewska et al.,
395 2018). Future studies will, however, demonstrate whether these findings open an exciting new avenue
396 for immunotherapy-based approaches in IPF.

397

398 **Limitations**

399 Despite analysing three independent timepoints, which cover the major stages of the bleomycin model,
400 some timepoints are still missing. However, we consciously wanted to reuse existing experiments and
401 avoid sacrifice of new animals. Future investigation would profit from an expansion, e.g. by inclusion
402 of existing measurements from other groups, to cover also the progression from the initial inflammation
403 towards active fibrosis phase by including analysis at day seven. Similarly, inflammatory profiling
404 during fibrosis resolution, i.e. after 28 or 35 days, would deliver valuable insights on the involvement
405 of specific subtypes during resolution. From a statistical point of view, the unbalanced study design
406 with differing sample numbers in subgroups is unfavourable, which complicates analysis and loses
407 some power. However, our use of robust methods such as NLME and machine learning methods
408 (random forest) were able to overcome these limitations. Although over a dozen independent
409 experimental runs were included, this is not a multi-centric study. Quantitative comparison of results
410 from other laboratories at other sites and other strains/substrains would allow to even better explore
411 bleomycin model system robustness and reproducibility. In this study, manual gating was used to
412 identify different cell populations, thereby including expert knowledge into the analysis and gating
413 specificity was confirmed shown by UMAP overlays. For some populations in the UMAP plots (e.g.
414 AM), the populations were more spread than expected, this was most likely due to do different marker
415 intensity (in this case CD11c) between different experimental runs. The topic of auto-gating is rapidly
416 developing and promises to considerably save hands-on time and foremost the potential to detect rare,
417 otherwise undetected cell subpopulations. The focus of this study was to primarily determine the
418 inflammatory cell kinetics, however to further unravel the role of inflammation and potential therapeutic
419 targets in fibrosis a quantified link of cell subpopulations to fibrotic processes is warranted.

420 **Recommendations**

421 This study explored fundamental aspects of the bleomycin animal model with good power owing to the
422 high sample numbers so that constructive recommendations can be inferred.

423 (I) In order to ascertain technical success of the experiment we strongly recommend to always include
424 a negative control (saline) and a positive control (bleomycin, transgenic or knock out otherwise
425 untreated) group with each $n \geq 8$. Foremost this serves to rate the strength of induced fibrosis and
426 technical quality of the experiment. Statistical power gain is very high for every added sample in the

427 single digit region. An $n\#$ of ≥ 8 leaves some safety margin to stay above the critical level of $n=5$ to
428 handle the occasional, unavoidable loss of samples due to premature death or technical problems.

429 (II) For more sensitive and pronounced inflammatory readouts BALF should be routinely sampled
430 together with lung tissue and both samples should be subjected to analogous analysis.

431 (III) For subsequent statistical analysis we strongly recommend to investigate distribution and potential
432 for improvements from data transformations and especially for multivariate methods additional centring
433 and scaling. We also recommend to use both multivariate and univariate, unsupervised and supervised
434 methods as they complement each other well in their type of generated insights.

435 **Conclusions**

436 The measurement of inflammatory cellular landscapes in the bleomycin-induced lung-injury mouse
437 model with flow cytometry is very robust and suitable to quantify kinetic changes in multiple cell
438 populations simultaneously. The results allowed to infer recommendations such as to add negative and
439 positive control, apply data pre-processing, combine multivariate and univariate methods and to
440 routinely also investigate BALF. We also found that the unintended development of potential substrains
441 does not per se hinder general reproducibility of results and the approach to adapt bleomycin doses to
442 the current experimental run is viable. This study underlines the relevance of combined analysis for
443 more holistic insights into inflammatory profile changes. Cell populations show quite distinct
444 trajectories in their kinetics. We also conclude that inflammatory cell-based response is active before,
445 during and after manifestation of fibrosis with a shift from the initial innate immune cell domination
446 towards the adaptive arm and inflammatory cell accumulation is not resolved after 3 weeks.

447

448 **Material and Methods**

449 **Animals**

450 All animal experiments were approved by the local authorities (Austrian Ministry of Science, Research
451 and Economics) (BMWF-66.010-0038-II-3b-2013, BMFW- 66.010/0038-WF/II/3b/2014,
452 BMFW-66.010/0049-WF/V/3b/2017, 66.010/0177-WF/3b/2017) and were performed in accordance
453 with relevant guidelines and regulations. Wild type groups of 15 independent experiments (unpublished
454 and published (Biasin et al., 2017)) were pooled and analysed. For each experimental run wild type
455 mice were obtained from Charles River or bred in-house in case of wild type littermates and are
456 annotated as separate strains. Overview of all strains and group sizes is given in Supplementary Table
457 S1. All mice were maintained with 12 h light/ dark cycles and they had access to water and standard
458 chow *ad libitum*.

459 **Bleomycin challenge and animal handling**

460 Male mice (25-30 g body weight) were anesthetized with isoflurane 2–2.5 % and intra-tracheal
461 administered with bleomycin (Sigma, Vienna, Austria) or saline solution (0.9 % w/v NaCl) using a
462 MicroSprayer® Aerosoliser (Penn-Century Inc., PA, Pennsylvania, USA), as previously described
463 (Biasin et al., 2020, 2017). Each bleomycin lot was titrated to give a comparable response for each
464 strain; dose range was 0.7-3.5 U/kg b.w., Supplementary Data 1). After bleomycin instillation, mice
465 were closely monitored till they completely recovered from anaesthesia. Bleomycin or saline solution
466 administration was performed once and animals were sacrificed after 3, 14 or 21 days.

467 **BALF and lung tissue preparation for flow cytometry**

468 Mice were euthanized via exsanguination and the lungs were perfused with phosphate buffered saline
469 (PBS; 137 mM NaCl, 2.7 mM KCl, 10 mM Na₂HPO₄, 1.8 mM KH₂PO₄, pH 7.2), through the right
470 ventricle. Mice were then lavaged with 1 ml PBS containing the Pierce protease inhibitor cocktail
471 (ThermoFisher Scientific, Vienna, Austria) and 1 mM EDTA. The obtained BALF was centrifuged,
472 washed with 1 ml MACS buffer (2 mM EDTA, 0.5 % BSA in 1X PBS), before being resuspended in
473 0.5 ml for cell counting and consequent FCM staining. Single cell lung tissue homogenates were
474 performed as previously described (Nagaraj et al., 2017). Briefly, the lower right lobe was weighed, cut
475 into approximately 1 mm pieces and digested with 0.7 mg/ml Collagenase and 30 µg/ml DNase in
476 RPMI medium supplemented with 10 % FCS, 2 mM glutamine and 1 % penicillin-streptomycin
477 (ThermoFisher Scientific) for 40 min at 37 °C with rotation at 350 rpm. The minced tissue was passed
478 through a 100 µm cell strainer to obtain a single cell suspension. In case of red blood cells
479 contamination, the cell suspension was treated with erythrolysis buffer (2.6 mM NH₄Cl, 0.09 M KCO₃,
480 0.6 M EDTA) for 5 min at room temperature. The number of live cells were counted using trypan blue

481 exclusion and then stained with fixable viability stain (ThermoFisher Scientific), washed and then fixed
482 with 1 % paraformaldehyde for 15 min on ice before being resuspended in MACS buffer.

483 **Flow cytometry**

484 Single cell suspensions were initially incubated with an Fc-receptor-binding antibody (ThermoFisher
485 Scientific) for 5 min on ice to prevent nonspecific binding. A master-mix containing one of two different
486 antibody combinations against cell surface markers (Supplementary Table S2) was added to the cells
487 incubated for 20 min at 4 °C. For each sample between 30'000 and 300'000 events were recorded on a
488 LSRII Flow Cytometer (BD Biosciences, Vienna, Austria) or Cytoflex S (Beckman Coulter, Vienna,
489 Austria). Samples were analysed either using FACSDiva (BD Biosciences) or FlowJo v10.6.2 (LLC,
490 Ashland, Oregon) software by users blinded to treatment condition. Cells were initially gated on FSC
491 and SSC characteristics and duplexes were removed using FSC-A / FSC-H dot blot, dead cells were
492 gated out using viability exclusion. Cells positive for the pan-leukocyte marker CD45 were taken for
493 further analysis, cell populations were identified using the gating strategy (Fig. 1C and Table 1), as
494 described in the results and based on published studies (Biasin et al., 2017; Gungl et al., 2018; Misharin
495 et al., 2017, 2013; Tighe et al., 2019b). A complete description of all antibodies is given in
496 Supplementary Table S2. Cell numbers are reported 10^5 in the BALF and 10^4 /mg tissue for the lung.
497 Uniform Manifold Approximation and Projection (UMAP) plots were performed in FlowJo, using
498 default settings (nearest neighbours 15, minimum distance value 0.5, Euclidean distance). First, fcs files
499 from at least three individual mice per analysis timepoint were downsampled to max 10'000 events and
500 then concatenated. Manually gated populations were then overlaid on UMAP plots to determine they
501 kinetics.

502 **Trichrome and immunofluorescence staining**

503 After BALF, the lungs were inflated with 4 % formalin via the trachea and then paraffin embedded.
504 Slides were cut at 2.5 μ m thick and stained with Masson's trichrome according to standard protocols.
505 Slides were scanned and imaged with a Virtual Slides VS120 Microscope and OlyVia Software (both
506 from Olympus, Vienna, Austria). For multi-colour immunofluorescence staining, 2.5 μ m paraffin-
507 embedded lung sections were dewaxed and subjected to heat induced antigen retrieval at pH6 (Perkin-
508 Elmer, Waltham, MA) using an antigen retrieval chamber for 15 min at 200 W. Slides were blocked
509 with Perkin-Elmer Antibody Block solution for 20 min in a humidified chamber, and primary antibodies
510 (Supplementary Table S3) were sequentially incubated o/n 4 °C in Perkin-Elmer Antibody Diluent.
511 After washing with TBS-T (274 mM NaCl, 47.6 mM Tris HCl + 2 % v/v Tween20 in H₂O) primary
512 antibodies against CD4, SiglecF and CD45 were detected with the Opal Polymer HRP secondary
513 antibody (Perkin-Elmer), using the Opal 540, 620, 690 substrates, respectively. Antibodies against
514 Collagen I, CD11c and CD45 were used simultaneously and detected with AlexaFluor-conjugated
515 secondary antibodies, donkey anti-goat AlexaFluor488, donkey anti-rabbit AlexaFluor555, chicken

516 anti-rat AlexaFluor647, respectively. Nuclear counterstaining was performed with DAPI solution
517 1 mg/ml (ThermoFisher Scientific).

518 **Confocal imaging**

519 For imaging immunofluorescence stained slides, a Leica TCS-SP8 (DMi8 inverted microscope with a
520 LIAchroic scan head) lightning confocal microscope was used (Leica, Wetzlar, Germany). The
521 acquisition process followed a “sequential workflow” with well-defined settings (shown in
522 Supplementary Table S4). In order to minimize fluorescent overlap the plugin “Channel Dye
523 Separation” of Leica Imaging system was used. The following objectives were used: Plan Fluotar
524 20x/0.75 multi immersion objective and Plan Fluotar 40x/1.25 glycerol immersion objective. Images
525 were acquired at 2048 x 2048 and a pixel size of 142 x 142nm.

526 **Statistical analysis**

527 Data visualisation and statistical analysis were performed with R v3.6.3 (R Core Team, 2020) (using
528 the packages readxl, openxlsx, plyr, stringr, tidyr, reshape, colorspace, RColorBrewer, ggplot2, ggpubr,
529 ggrepel, gridExtra, magrittr, cowplot, plotly, lemon, lawstat, dendsort, pheatmap, cellWise, missMDA,
530 FactoMineR, nlme, emmeans, MetaboAnalystR 2.0, caret, randomForest, randomForestExplainer,
531 partykit, e1071), TIBCO Spotfire v10.9.0, TIBCO, Palo Alto, CA and FlowJo v10 (LLC, Ashland,
532 Oregon). Animals with >30% missing values in the investigated 16 cells populations were excluded
533 from the analysis.

534 All reported p-values were adjusted for multiple testing according to Benjamini-Hochberg (BH)
535 denoted as p_{BH} (R function *p.adjust*). Distribution and scedasticity were investigated with Kolmogorov-
536 Smirnov test and Brown-Forsythe Levene-type test, respectively (p_{BH} Supplementary Data 1). Seven
537 common transformations were tested: square root, reciprocal, Freeman Tukey, logit (on counts mapped
538 to 0.25-0.75), LOG, LOG_{x+1} , 4RT (Supplementary Fig. S1).

539 Principal component analysis (PCA) analysis (R function *prcomp*) was performed centred and scaled
540 to unit variance (z-scaled) on total cell counts (untransformed, LOG_{x+1} or 4RT transformed). The dataset
541 (303 samples, 16 cell populations) contained no missing values and 1.3 % zeros. MacroPCA analysis
542 (R function *MacroPCA*) was performed centred and scaled to unit variance on total cell counts
543 (untransformed, LOG_{x+1} or 4RT transformed). The number of components was set to cumulatively
544 retain 80 % of explained variance, but to deliver between two and ten components. Hierarchical
545 clustering analysis was performed centred and scaled to unit variance (R function *scale*) on total cell
546 counts, for untransformed data per cell type than samples. LOG_{x+1} or 4RT data was centred and scaled
547 only per cell type. The dendrograms were clustered by Lance-Williams dissimilarity update with
548 complete linkage (R function *dist* and *hclust*) and sorted (R function *dendsort*) at every merging point

549 according to the average distance of subtrees and plotted at the corresponding heat maps (R function
550 *pheatmap*).

551 Non-linear mixed models were fitted (R function simple models *gls* or mixed models *lme* with
552 maximum likelihood (ML), with LOG_{x+1} transformation and no longitudinal covariance applied (mice
553 were sacrificed at each time point). Model selection was based on the forward addition approach and
554 complex models were rechecked by backward dropping of factors. Simple models were constructed
555 using the forward addition approach incorporating the fixed factors *Treatment* {Saline,Bleo}, *Day*
556 {3,14,21} post treatment and the mouse background, *Substrain* {A,B,C,D,E}. The interactions,
557 *Treatment:Substrain* and *Treatment:Day* were include to determine whether the treatment effect
558 depended on the *Substrain* or *Day*. Mixed models additionally included the experimental ID as a random
559 factor (~1|Exp_ID). Complex mixed models were created by combining mixed models with the
560 interactions *Treatment:Substrain* and/or *Treatment:Day*. Models were then simplified by merging all
561 saline samples into one control group generating the simple model [*SalineDay+Substrain*] and by
562 including *Exp_ID* as a random factor the mixed model [*SalineDay+Substrain~1| Exp_ID*]. Due to rank
563 deficiencies arising from the unbalanced design the model *SalineDay:Substrain* was not possible.
564 Criteria for model performance and suitability were lower AIC (Akaike information criterion; relative
565 estimate of information loss), higher log-likelihood (goodness of fit), significance in log likelihood ratio
566 test comparing two models, quality of Q-Q plots and randomness in residual^[Box 2] plots (Supplementary
567 Data 1 and Supplementary Fig. S2). Post-hoc pairwise comparisons were readout as back transformed
568 estimates (R function *emmeans*, type = “response”) with $p_{BH} \leq 0.05$ being considered statistically
569 significant.

570 Orthogonal projections to latent structures discriminant analysis (OPLS-DA) on LOG_{x+1} data was
571 performed centred and scaled to unit variance (R function *Normalization* with scaleNorm=”AutoNorm”
572 and R function *OPLSR.Anal*) with a standard 7-fold cross validation for the classification factor
573 *SalineDay*. Model stability was additionally verified with 1000 random label permutations.

574 Conditional inference trees were fit with default settings (R function *ctree*) which limits tree size to
575 include only significant splits avoiding overfitting, so that no further cross-validation or pruning was
576 applied. The random forest (R function *randomForest*) error rates decrease markedly within the first
577 100 trees and stabilized fully after 1500 to 2500 trees. All reported random forests grown with 5000
578 trees to guarantee stability and hyperparameter, mtry (8 in BALF and 2 in lung) was tuned to minimal
579 out-of-bag errors (OOB) (R function *tuneRF*). The model stability and prediction quality (R function
580 *confusionMatrix*) of conditional inference trees and random forest was evaluated by splitting the
581 LOG_{x+1} randomly into trainings/test set (65 % / 35 %) stratified for the classification factor *SalineDay*
582 (R function *createDataPartition*).

583

584 **Author contributions**

585 Conceptualisation, Data curation, Software, Validation, Methodology, N.B. and L.M.M.; Formal
586 analysis and Visualisation N.B., D.S., F.V., and L.M.M.; Investigation, V.B., D.S., F.V., K.J., B.M.N.,
587 N.S. and L.M.M.; Resources, V.B., D.S., F.V., K.J., B.M.N., N.S., G.K. and L.M.M.; Writing – original
588 draft, N.B., V.B., G.K., M.W., L.M.M.; Writing – Review & Editing, all authors; Project administration,
589 Supervision and Funding acquisition, G.K. and L.M.M.

590 **Acknowledgements**

591 We are very grateful for the technical assistance from Kerstin Schweighofer, Sabine Halsegger, Thomas
592 Fuchs, Nina Treitler, Eva Grasmann, Camilla Götz, and Betty Schrenk, as well as Slaven Crnkovic,
593 Mathias Hochgerner, Chandran Nagaraj and Horst Olschewski for the valuable discussions and advice.
594 Diana Schnögl, Francesco Valzano and Neha Sharma are members of the MolMed graduate
595 programme. Diana Schnögl is funded by FFG, project number 870904 awarded to Leigh Marsh.
596 Francesco Valzano is funded by FFG, project number 874229 awarded to Grazyna Kwapiszewska.
597 Valentina Biasin is funded by Austrian Science Fund (FWF; project number, T1032-B34).

598 **Competing interests**

599 The authors declare that they have no competing interests.

600 **Data and materials availability**

601 All data needed to evaluate the conclusions in the paper are present in the paper or the Supplementary
602 Materials.

603

604

605 **References**

- 606 Aran D, Looney AP, Liu L, Wu E, Fong V, Hsu A, Chak S, Naikawadi RP, Wolters PJ, Abate AR,
607 Butte AJ, Bhattacharya M. 2019. Reference-based analysis of lung single-cell sequencing reveals
608 a transitional profibrotic macrophage. *Nat Immunol* **20**:163–172. doi:10.1038/s41590-018-0276-
609 y
- 610 B Moore B, Lawson WE, Oury TD, Sisson TH, Raghavendran K, Hogaboam CM. 2013. Animal models
611 of fibrotic lung disease. *Am J Respir Cell Mol Biol* **49**:167–79. doi:10.1165/rcmb.2013-0094TR
- 612 Balestro E, Calabrese F, Turato G, Lunardi F, Bazzan E, Marulli G, Biondini D, Rossi E, Sanduzzi A,
613 Rea F, Rigobello C, Gregori D, Baraldo S, Spagnolo P, Cosio MG, Saetta M. 2016. Immune
614 Inflammation and Disease Progression in Idiopathic Pulmonary Fibrosis. *PLoS One* **11**:e0154516.
615 doi:10.1371/journal.pone.0154516
- 616 Biasin V, Crnkovic S, Sahu-Osen A, Birnhuber A, El Agha E, Sinn K, Klepetko W, Olschewski A,
617 Bellusci S, Marsh LM, Kwapiszewska G. 2020. PDGFR α and α SMA mark two distinct
618 mesenchymal cell populations involved in parenchymal and vascular remodeling in pulmonary
619 fibrosis. *Am J Physiol Cell Mol Physiol* ajplung.00128.2019. doi:10.1152/ajplung.00128.2019
- 620 Biasin V, Wygrecka M, Marsh LM, Becker-Pauly C, Brcic L, Ghanim B, Klepetko W, Olschewski A,
621 Kwapiszewska G. 2017. Meprin β contributes to collagen deposition in lung fibrosis. *Sci Rep*
622 **7**:39969. doi:10.1038/srep39969
- 623 Cui H, Jiang D, Banerjee S, Xie N, Kulkarni T, Liu R-M, Duncan SR, Liu G. 2020. Monocyte-derived
624 alveolar macrophage Apolipoprotein E participates in pulmonary fibrosis resolution. *JCI Insight*.
625 doi:10.1172/jci.insight.134539
- 626 Della Latta V, Cecchetti A, Del Ry S, Morales MA. 2015. Bleomycin in the setting of lung fibrosis
627 induction: From biological mechanisms to counteractions. *Pharmacol Res* **97**:122–130.
628 doi:10.1016/j.phrs.2015.04.012
- 629 El Agha E, Kramann R, Schneider RK, Li X, Seeger W, Humphreys BD, Bellusci S. 2017.
630 Mesenchymal Stem Cells in Fibrotic Disease. *Cell Stem Cell*. doi:10.1016/j.stem.2017.07.011
- 631 Engblom C, Pflirschke C, Zilionis R, Da Silva Martins J, Bos SA, Courties G, Rickelt S, Severe N,
632 Baryawno N, Faget J, Savova V, Zemmour D, Kline J, Siwicki M, Garris C, Pucci F, Liao HW,
633 Lin YJ, Newton A, Yaghi OK, Iwamoto Y, Tricot B, Wojtkiewicz GR, Nahrendorf M, Cortez-
634 Retamozo V, Meylan E, Hynes RO, Demay M, Klein A, Bredella MA, Scadden DT, Weissleder
635 R, Pittet MJ. 2017. Osteoblasts remotely supply lung tumors with cancer-promoting SiglecFhigh
636 neutrophils. *Science (80-)* **358**. doi:10.1126/science.aal5081
- 637 Gungl A, Biasin V, Wilhelm J, Olschewski A, Kwapiszewska G, Marsh LM. 2018. Fra2
638 Overexpression in Mice Leads to Non-allergic Asthma Development in an IL-13 Dependent
639 Manner. *Front Immunol* **9**:2018. doi:10.3389/fimmu.2018.02018
- 640 Hubert M, Rousseeuw PJ, Van den Bossche W. 2019. MacroPCA: An All-in-One PCA Method

- 641 Allowing for Missing Values as Well as Cellwise and Rowwise Outliers. *Technometrics* 1–18.
642 doi:10.1080/00401706.2018.1562989
- 643 Izbicki G, Segel MJ, Christensen TG, Conner MW, Breuer R. 2002. Time course of bleomycin-induced
644 lung fibrosis. *Int J Exp Pathol* **83**:111–9. doi:10.1046/j.1365-2613.2002.00220.x
- 645 Joshi N, Watanabe S, Verma R, Jablonski RP, Chen CI, Cheres P, Markov NS, Reyfman PA,
646 McQuattie-Pimentel AC, Sichizya L, Lu Z, Piseaux-Aillon R, Kirchenbuechler D, Flozak AS,
647 Gottardi CJ, Cuda CM, Perlman H, Jain M, Kamp DW, Budinger GRS, Misharin A V. 2020. A
648 spatially restricted fibrotic niche in pulmonary fibrosis is sustained by M-CSF/M-CSFR signalling
649 in monocyte-derived alveolar macrophages. *Eur Respir J* **55**. doi:10.1183/13993003.00646-2019
- 650 Kahloon RA, Xue J, Bhargava A, Csizmadia E, Otterbein L, Kass DJ, Bon J, Soejima M, Levesque
651 MC, Lindell KO, Gibson KF, Kaminski N, Banga G, Oddis C V., Pilewski JM, Sciruba FC,
652 Donahoe M, Zhang Y, Duncan SR. 2013. Patients with Idiopathic Pulmonary Fibrosis with
653 Antibodies to Heat Shock Protein 70 Have Poor Prognoses. *Am J Respir Crit Care Med* **187**:768–
654 775. doi:10.1164/rccm.201203-0506OC
- 655 Kurosu K, Takiguchi Y, Okada O, Yumoto N, Sakao S, Tada Y, Kasahara Y, Tanabe N, Tatsumi K,
656 Weiden M, Rom WN, Kuriyama T. 2008. Identification of Annexin 1 as a Novel Autoantigen in
657 Acute Exacerbation of Idiopathic Pulmonary Fibrosis. *J Immunol* **181**:756–767.
658 doi:10.4049/jimmunol.181.1.756
- 659 Kwapiszewska G, Gungl A, Wilhelm J, Marsh LM, Puthenparampil HT, Sinn K, Didiasova M,
660 Klepetko W, Kosanovic D, Schermuly RT, Wujak L, Weiss B, Schaefer L, Schneider M, Kreuter
661 M, Olschewski A, Seeger W, Olschewski H, Wygrecka M. 2018. Transcriptome profiling reveals
662 the complexity of pirfenidone effects in idiopathic pulmonary fibrosis. *Eur Respir J* **52**.
663 doi:10.1183/13993003.00564-2018
- 664 Maher TM, Strek ME. 2019. Antifibrotic therapy for idiopathic pulmonary fibrosis: time to treat. *Respir*
665 *Res* **20**:205. doi:10.1186/s12931-019-1161-4
- 666 Marchal-Sommé J, Uzunhan Y, Marchand-Adam S, Valeyre D, Soumelis V, Crestani B, Soler P. 2006.
667 Cutting Edge: Nonproliferating Mature Immune Cells Form a Novel Type of Organized
668 Lymphoid Structure in Idiopathic Pulmonary Fibrosis. *J Immunol* **176**:5735–5739.
669 doi:10.4049/jimmunol.176.10.5735
- 670 Marsh LM, Jandl K, Grünig G, Foris V, Bashir M, Ghanim B, Klepetko W, Olschewski H, Olschewski
671 A, Kwapiszewska G. 2018. The inflammatory cell landscape in the lungs of patients with
672 idiopathic pulmonary arterial hypertension. *Eur Respir J* **51**:1701214.
673 doi:10.1183/13993003.01214-2017
- 674 Marshall DC, Saliccioli JD, Shea BS, Akuthota P. 2018. Trends in mortality from idiopathic
675 pulmonary fibrosis in the European Union: an observational study of the WHO mortality database
676 from 2001–2013. *Eur Respir J* **51**:1701603. doi:10.1183/13993003.01603-2017
- 677 McCubbrey AL, Barthel L, Mohning MP, Redente EF, Mould KJ, Thomas SM, Leach SM, Danhorn T,

- 678 Gibbings SL, Jakubzick C V., Henson PM, Janssen WJ. 2018. Deletion of c-FLIP from CD11b^{hi}
679 Macrophages Prevents Development of Bleomycin-induced Lung Fibrosis. *Am J Respir Cell Mol*
680 *Biol* **58**:66–78. doi:10.1165/rcmb.2017-0154OC
- 681 Meltzer EB, Noble PW. 2008. Idiopathic pulmonary fibrosis. *Orphanet J Rare Dis* **3**:8.
682 doi:10.1186/1750-1172-3-8
- 683 Misharin A V., Morales-Nebreda L, Mutlu GM, Budinger GRS, Perlman H. 2013. Flow Cytometric
684 Analysis of Macrophages and Dendritic Cell Subsets in the Mouse Lung. *Am J Respir Cell Mol*
685 *Biol* **49**:503–510. doi:10.1165/rcmb.2013-0086MA
- 686 Misharin A V., Morales-Nebreda L, Reyfman PA, Cuda CM, Walter JM, McQuattie-Pimentel AC,
687 Chen C-I, Anekalla KR, Joshi N, Williams KJN, Abdala-Valencia H, Yacoub TJ, Chi M, Chiu S,
688 Gonzalez-Gonzalez FJ, Gates K, Lam AP, Nicholson TT, Homan PJ, Soberanes S, Dominguez S,
689 Morgan VK, Saber R, Shaffer A, Hinchcliff M, Marshall SA, Bharat A, Berdnikovs S, Bhorade
690 SM, Bartom ET, Morimoto RI, Balch WE, Sznajder JI, Chandel NS, Mutlu GM, Jain M, Gottardi
691 CJ, Singer BD, Ridge KM, Bagheri N, Shilatifard A, Budinger GRS, Perlman H. 2017. Monocyte-
692 derived alveolar macrophages drive lung fibrosis and persist in the lung over the life span. *J Exp*
693 *Med* **214**:2387–2404. doi:10.1084/jem.20162152
- 694 Nagaraj C, Haitchi HM, Heinemann A, Howarth PH, Olschewski A, Marsh LM. 2017. Increased
695 Expression of p22phox Mediates Airway Hyperresponsiveness in an Experimental Model of
696 Asthma. *Antioxid Redox Signal* **27**:1460–1472. doi:10.1089/ars.2016.6863
- 697 Ogushi F, Tani K, Endo T, Tada H, Kawano T, Asano T, Huang L, Ohmoto Y, Muraguchi M, Moriguchi
698 H, Sone S. 2001. Autoantibodies to IL-1 alpha in sera from rapidly progressive idiopathic
699 pulmonary fibrosis. *J Med Invest* **48**:181–9.
- 700 Peng R, Sridhar S, Tyagi G, Phillips JE, Garrido R, Harris P, Burns L, Renteria L, Woods J, Chen L,
701 Allard J, Ravindran P, Bitter H, Liang Z, Hogaboam CM, Kitson C, Budd DC, Fine JS, Bauer
702 CMT, Stevenson CS. 2013. Bleomycin Induces Molecular Changes Directly Relevant to
703 Idiopathic Pulmonary Fibrosis: A Model for “Active” Disease. *PLoS One* **8**:e59348.
704 doi:10.1371/journal.pone.0059348
- 705 R Core Team. 2020. R: A language and environment for statistical computing. R Foundation for
706 Statistical Computing.
- 707 Reyfman PA, Walter JM, Joshi N, Anekalla KR, McQuattie-Pimentel AC, Chiu S, Fernandez R,
708 Akbarpour M, Chen C-I, Ren Z, Verma R, Abdala-Valencia H, Nam K, Chi M, Han S, Gonzalez-
709 Gonzalez FJ, Soberanes S, Watanabe S, Williams KJN, Flozak AS, Nicholson TT, Morgan VK,
710 Winter DR, Hinchcliff M, Hrusch CL, Guzy RD, Bonham CA, Sperling AI, Bag R, Hamanaka
711 RB, Mutlu GM, Yeldandi A V., Marshall SA, Shilatifard A, Amaral LAN, Perlman H, Sznajder
712 JI, Argento AC, Gillespie CT, Dematte J, Jain M, Singer BD, Ridge KM, Lam AP, Bharat A,
713 Bhorade SM, Gottardi CJ, Budinger GRS, Misharin A V. 2019. Single-Cell Transcriptomic
714 Analysis of Human Lung Provides Insights into the Pathobiology of Pulmonary Fibrosis. *Am J*

- 715 *Respir Crit Care Med* **199**:1517–1536. doi:10.1164/rccm.201712-2410OC
- 716 Rousseeuw PJ, Hubert M. 2018. Anomaly detection by robust statistics. *Wiley Interdiscip Rev Data*
- 717 *Min Knowl Discov* **8**:e1236. doi:10.1002/widm.1236
- 718 Saeys Y, Van Gassen S, Lambrecht BN. 2016. Computational flow cytometry: helping to make sense
- 719 of high-dimensional immunology data. *Nat Rev Immunol* **16**:449–462. doi:10.1038/nri.2016.56
- 720 Selman M, King TE, Pardo A. 2001. Idiopathic Pulmonary Fibrosis: Prevailing and Evolving
- 721 Hypotheses about Its Pathogenesis and Implications for Therapy. *Ann Intern Med* **134**:136.
- 722 doi:10.7326/0003-4819-134-2-200101160-00015
- 723 Selman M, Pardo A. 2002. Idiopathic pulmonary fibrosis: an epithelial/fibroblastic cross-talk disorder.
- 724 *Respir Res* **3**:3. doi:10.1186/RR175
- 725 Taillé C, Grootenboer-Mignot S, Boursier C, Michel L, Debray M-P, Fagart J, Barrientos L, Mailleux
- 726 A, Cigna N, Tubach F, Marchal-Sommé J, Soler P, Chollet-Martin S, Crestani B. 2011.
- 727 Identification of Periplakin as a New Target for Autoreactivity in Idiopathic Pulmonary Fibrosis.
- 728 *Am J Respir Crit Care Med* **183**:759–766. doi:10.1164/rccm.201001-0076OC
- 729 Tashiro J, Rubio GA, Limper AH, Williams K, Elliot SJ, Ninou I, Aidinis V, Tzouveleakis A, Glassberg
- 730 MK. 2017. Exploring animal models that resemble idiopathic pulmonary fibrosis. *Front Med*.
- 731 doi:10.3389/fmed.2017.00118
- 732 Tighe RM, Misharin A V., Jakubzick C V., Brinkman R, Curtis JL, Duggan R, Freeman CM, Herold
- 733 S, Janssen W, Nakano H, Redente EF, Singer BD, Sperling AI, Swaminathan S, Yu YR, Zacharias
- 734 WJ. 2019a. Improving the quality and reproducibility of flow cytometry in the lung. *Am J Respir*
- 735 *Cell Mol Biol* **61**:150–161. doi:10.1165/rcmb.2019-0191ST
- 736 Tighe RM, Misharin A V., Jakubzick C V., Brinkman R, Curtis JL, Duggan R, Freeman CM, Herold
- 737 S, Janssen W, Nakano H, Redente EF, Singer BD, Sperling AI, Swaminathan S, Yu YR, Zacharias
- 738 WJ. 2019b. Improving the quality and reproducibility of flow cytometry in the lung. *Am J Respir*
- 739 *Cell Mol Biol* **61**:150–161. doi:10.1165/rcmb.2019-0191ST
- 740 Todd NW, Scheraga RG, Galvin JR, Iacono AT, Britt EJ, Luzina IG, Burke AP, Atamas SP. 2013.
- 741 Lymphocyte aggregates persist and accumulate in the lungs of patients with idiopathic pulmonary
- 742 fibrosis. *J Inflamm Res* **6**:63–70. doi:10.2147/JIR.S40673
- 743 Wuyts WA, Agostini C, Antoniou KM, Bouros D, Chambers RC, Cottin V, Egan JJ, Lambrecht BN,
- 744 Lories R, Parfrey H, Prasse A, Robalo-Cordeiro C, Verbeke E, Verschakelen JA, Wells AU,
- 745 Verleden GM. 2013. The pathogenesis of pulmonary fibrosis: a moving target. *Eur Respir J*
- 746 **41**:1207–18. doi:10.1183/09031936.00073012
- 747 Xie T, Wang Y, Deng N, Huang G, Taghavifar F, Geng Y, Liu N, Kulur V, Yao C, Chen P, Liu Z,
- 748 Stripp B, Tang J, Liang J, Noble PW, Jiang D. 2018. Single-Cell Deconvolution of Fibroblast
- 749 Heterogeneity in Mouse Pulmonary Fibrosis. *Cell Rep* **22**:3625–3640.
- 750 doi:10.1016/j.celrep.2018.03.010

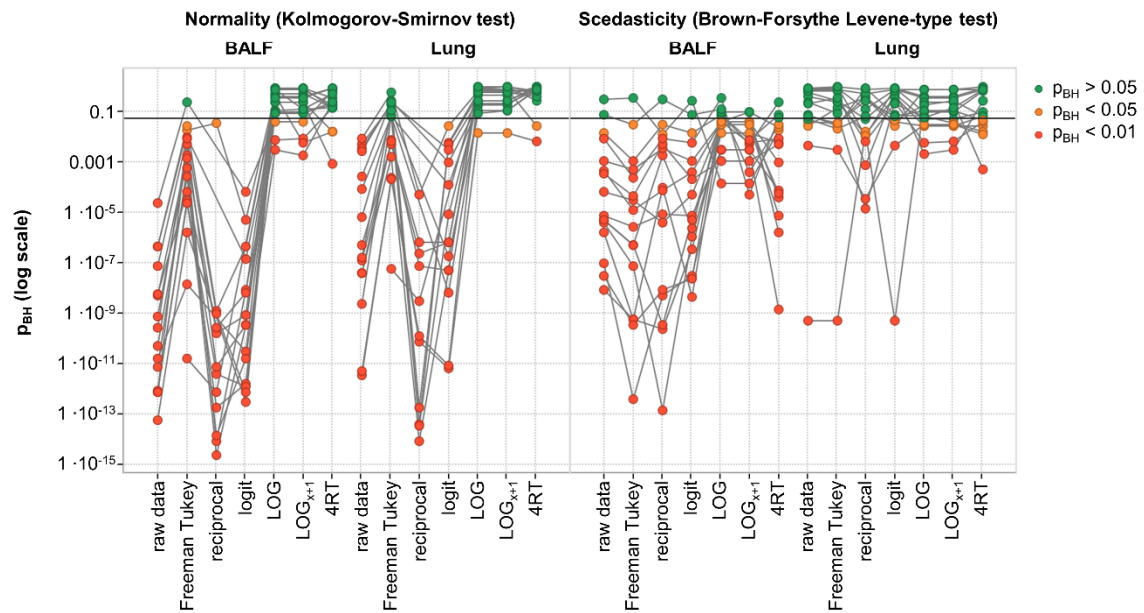
751 **Supplementary Figures and Tables**

A

| transformation | equation |
|----------------|--|
| square root | $\sqrt[2]{x}$ |
| reciprocal | $\frac{1}{x}$ |
| Freeman Tukey | $\sqrt[2]{x} + \sqrt[2]{x+1}$ |
| logit | $\ln\left(\frac{x_{map}}{(1-x_{map})}\right)$ with $x_{map} = \frac{(x-Y_{lwr}) \cdot ((upr-d) - (lwr-d))}{(Y_{upr}-Y_{lwr})} + d$ BALF $Y_{upr} = 30 \cdot 10^5$, lung $Y_{upr} = 15 \cdot 10^4$, $Y_{lwr} = 0$, $upr = 1$, $lwr = 0$, $d = 0.25$ |
| LOG | $\log_{10}(x)$ |
| LOGx+1 | $\log_{10}(x+1)$ |
| 4RT | $\sqrt[4]{x}$ |

x – cell counts (BALF 10^5 , lung 10^4 /mg tissue)

B

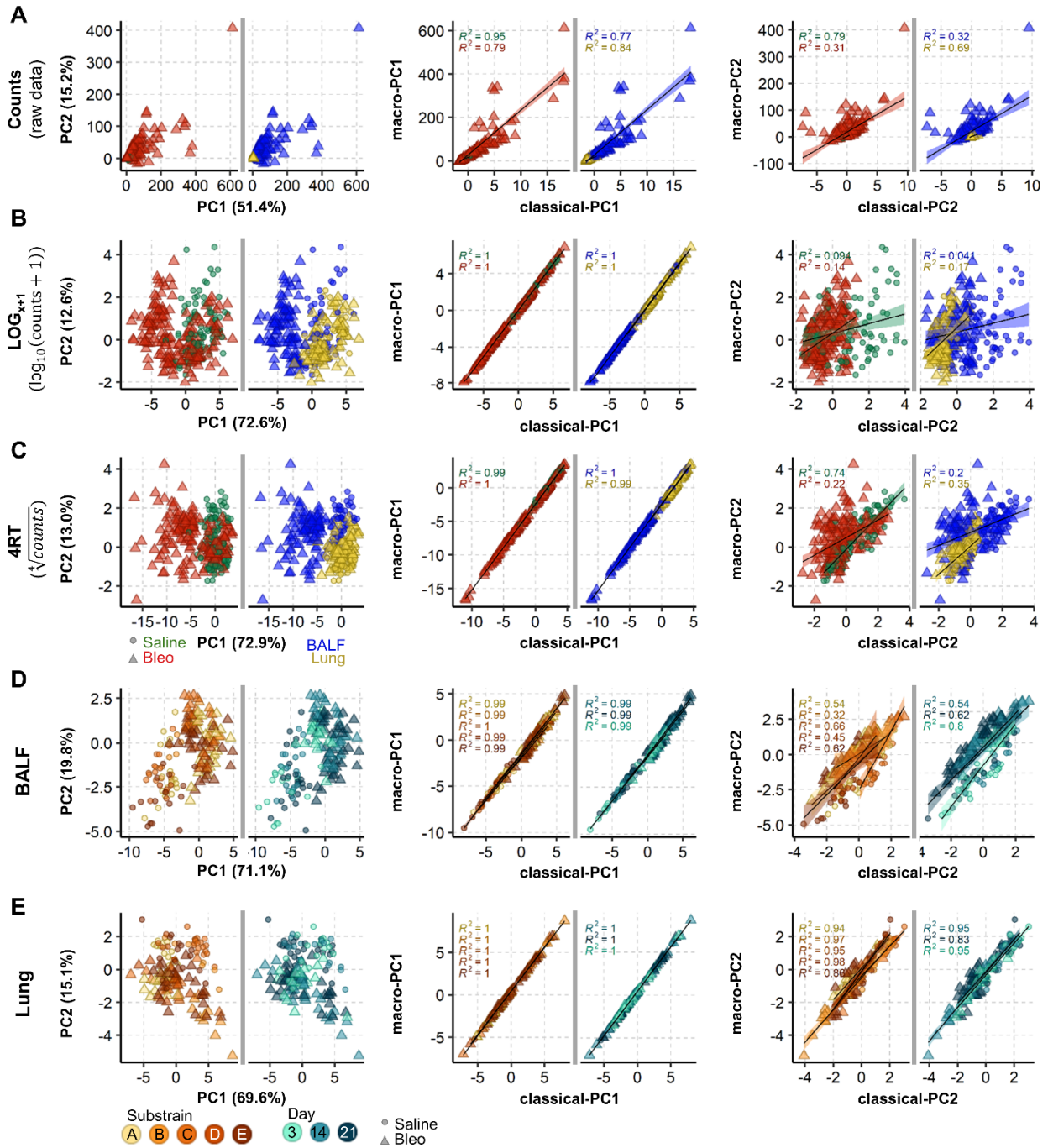


752

753 **Fig. S1.** Data transformations improve distribution and scedasticity. (A) List of tested data transformations with equations. (B)

754 Normality and scedasticity was tested for each of the 16 cell populations in either 159 BALF or 144 lung samples for

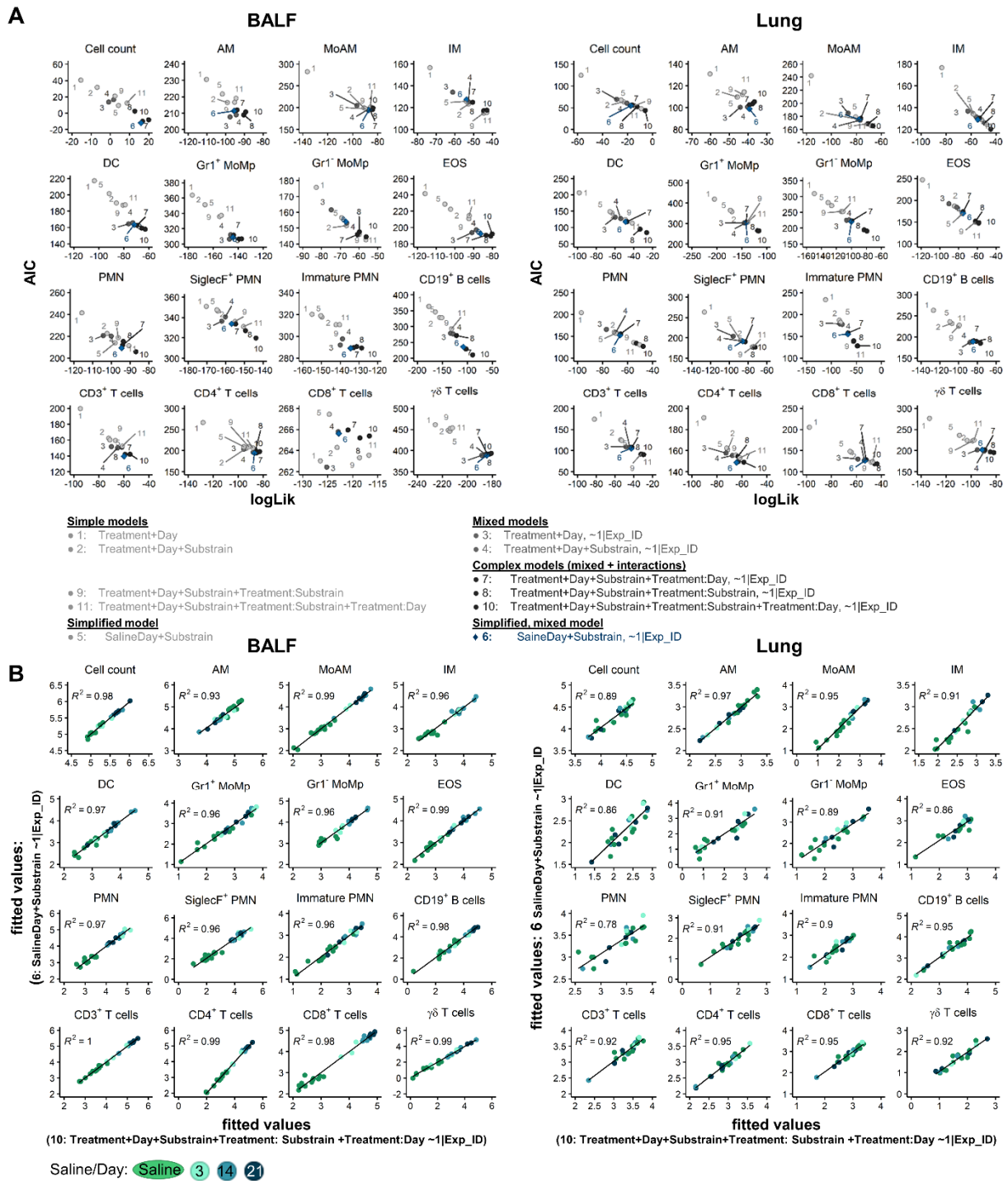
755 each of the transformations. The horizontal line denotes pBH= 0.05.



756

757 **Fig. S2.** MacroPCA and PCA deliver similar results. (A-C) MacroPCA scores plot of combined BALF (159 samples) and lung
 758 tissue (144 samples), before (untransformed, (A)) and after data transformation by LOG_{x+1} (B) or 4RT (fourth root;
 759 (C)). Samples are coloured to highlight effect of bleomycin (Saline or Bleo) and compartment (BALF or Lung). Middle
 760 and right panels show the linear fit of the first two principal components derived from the macroPCA and PCA results.
 761 (D-E) Separation of entire LOG_{x+1} transformed dataset into the tissue compartments, BALF (D) and lung (E). Middle
 762 and right panels show the linear fit of the first two principal components derived from the macroPCA and PCA results.
 763 Samples are coloured to highlight different days and substrains. Shapes are in all plots circles for saline and triangles
 764 for bleomycin.

765



766

767

768

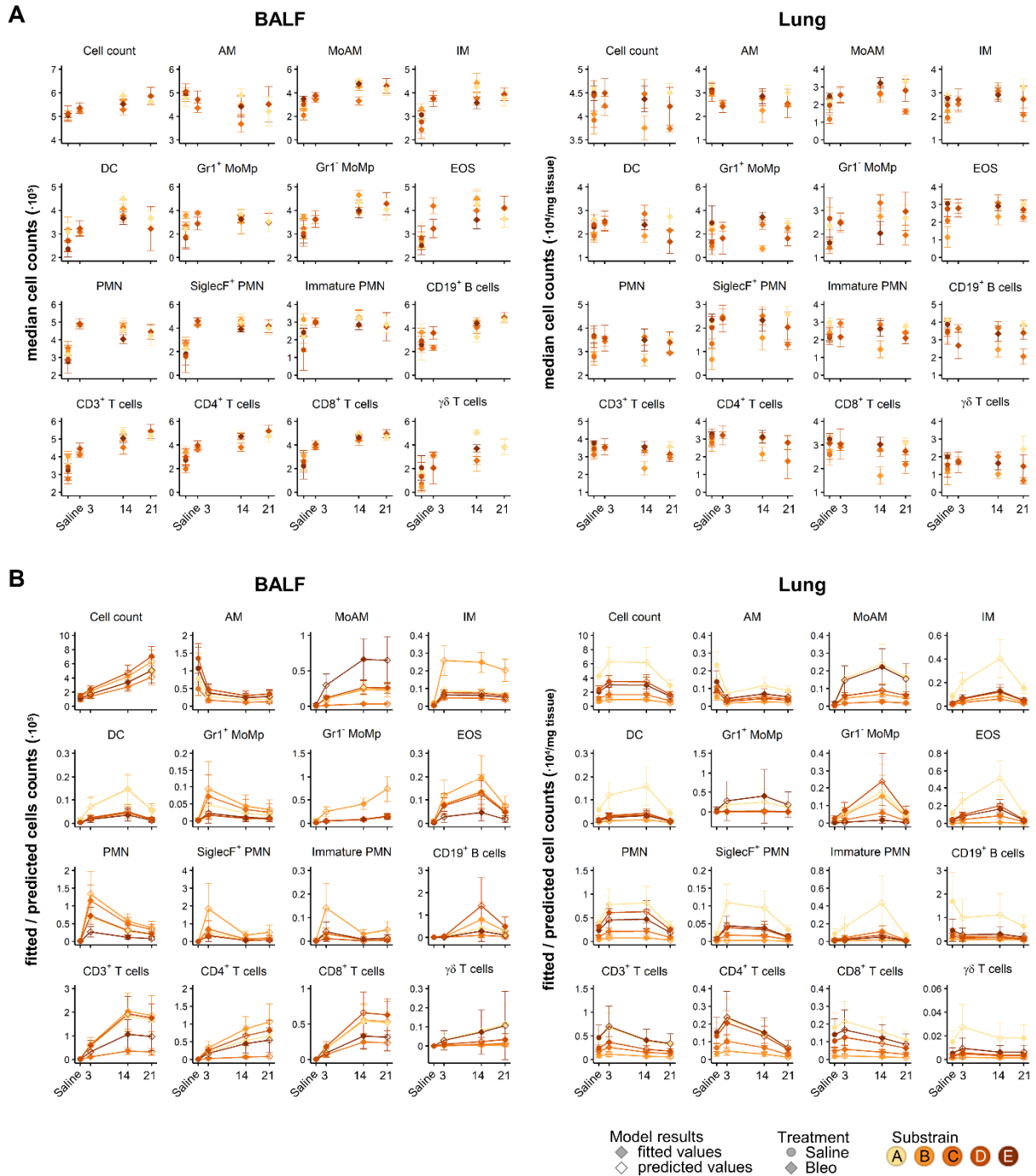
769

770

771

772

Fig. S3. Simplified mixed models exhibit best performance. Overview of ANOVA model performances for model selection by: (A) Comparison of model performance by AIC and logLik for all 16 cell populations in BALF and lung, better performance is indicated by lower relative estimate of information loss (AIC; Akaike information criterion) and higher goodness of fit (log-likelihood, logLik). (B) Direct comparison of fitted values (on LOG_{x+1} scale) of the simplified mixed model versus the most complex mixed model. The Pearson correlation is shown as black line and R² is given.



773

774

775

776

777

778

Fig. S4. Modelling of 16 cell populations in 159 BALF or 144 lung samples reveals complex cell kinetics. Overview of ANOVA model performances for model selection by: A) Plot of mean cell counts at each time point for each substrain and their standard deviation, coloured according to each substrain. B) Plot of LOG_{x+1} back transformed, fitted or predicted mean cell counts for each substrain and their standard errors from non-linear mixed models [$\text{SalineDay} + \text{Substrain}, \sim | \text{Exp_ID} |$] from cell counts (BALF $\cdot 10^5$, lung $\cdot 10^4/\text{mg tissue}$).

779

780 **Supplementary Table S1. Overview of group distribution.**

| Substrain | A | | B | | C | | D | | E | |
|-----------|-------------------|---------------|-------------------|---------------|---------------|---------------|---------------|---------------|---------------|---------------|
| | BALF | Lung | BALF | Lung | BALF | Lung | BALF | Lung | BALF | Lung |
| | Saline Bleo | Saline Bleo | Saline Bleo | Saline Bleo | Saline Bleo | Saline Bleo | Saline Bleo | Saline Bleo | Saline Bleo | Saline Bleo |
| Day 3 | | | | | 8 11 | 8 12 | | | 5 8 3 4 | 5 7 3 4 |
| Day 14 | 4 4 | | 0 4 0 8 5 0 | 0 9 7 0 | 7 13 | 4 13 | 6 10 | 6 10 | | |
| Day 21 | 5 7 5 9 5 7 | 5 9 5 7 | | | | 6 3 | | | 3 6 4 8 | 3 6 4 8 |

781

782 **Supplementary Table S2. Antibodies, fluorophores and sources for flow cytometry.**

| Panel | Antigen | Label | Company | Catalogue | Clone | Isotype | Identifier | Dilution |
|----------|------------------|-------------|---------------|------------|-------------|----------------------|-------------|----------|
| Myeloid | CD45 | FITC | Thermo Fisher | 11-0451-82 | 30-F11 | Rat IgG2b, κ | AB_2753206 | 1:200 |
| | SiglecF | PE | BD Bioscience | 562757 | E50-2440 | Rat IgG2a, κ | AB_2687994 | 1:20 |
| | CD11c | ef450 | Thermo Fisher | 48-0114-82 | N418 | Armenian hamster IgG | AB_1548654 | 1:50 |
| | CD11b | ef506 | Thermo Fisher | 69-0112-82 | M1/70 | Rat IgG2b, κ | AB_2637406 | 1:50 |
| | Gr-1 (Ly6G/Ly6C) | PE-Cy7 | Biologend | 108402 | RB6-8C5 | Rat IgG2b, κ | AB_313367 | 1:800 |
| | CD64a/b | AF647 | BD Bioscience | 558539 | X54-5/7.1 | Mouse NOD/Lt IgG1, κ | AB_647120 | 1:20 |
| | CD24 | PerCP Cy5.5 | BD Bioscience | 562360 | M1/69 | Rat IgG2b, κ | AB_11151895 | 1:500 |
| | MHC-II | APC-Cy7 | Biologend | 107628 | M5/114.15.2 | Rat IgG2b, κ | AB_2069377 | 1:400 |
| Lymphoid | CD45 | PerCP Cy5.5 | eBioscience | 45-0451-82 | 30-F11 | Rat IgG2b, κ | AB_1107002 | 1:200 |
| | CD3 | AF700 | Thermo Fisher | 56-0033-82 | eBio500A2 | Syrian hamster / IgG | AB_837094 | 1:50 |
| | CD19 | BB515 | BD Bioscience | 564531 | 1D3 | Rat IgG2a, κ | AB_2738836 | 1:50 |
| | CD8 | PE | Biologend | 100708 | 53-6.7 | Rat IgG2a, κ | AB_312747 | 1:100 |
| | CD4 | APC | Biologend | 17-0041-82 | GK1.5 | Rat IgG2b, κ | AB_469320 | 1:100 |
| | gdTCR | ef450 | Thermo Fisher | 48-5711-82 | eBioGL3 | Armenian hamster IgG | AB_2574071 | 1:50 |

783

784 **Supplementary Table S3. Antibodies, fluorophores and sources for immunofluorescent staining.**

| Antigen | Host | Brand | Catalogue | Identifier | Concentration (µg/ml) |
|------------|--------|------------------|------------|------------|-----------------------|
| Collagen I | Goat | Southern Biotech | 1310-01 | AB_2753206 | 0.8 |
| CD4 | Rat | Synaptic Systems | HS-360 017 | AB_2800530 | 10 |
| CD11c | Rabbit | Thermo Fisher | PA5-79537 | AB_2746652 | 3.3 |
| SiglecF | Goat | R&D Systems | AF1706 | AB_354943 | 0.4 |
| Ly6G | Rat | Biologend | 127601 | AB_1089179 | 3.3 |
| CD45 | Rabbit | Abcam | AB10558 | AB_442810 | 0.6 |

785

786

787 **Supplementary Table S4. Instrument configurations.**

| Instrument | Laser lines | Bandpass Filters | | | | | | |
|-------------------|--------------------|-------------------------|--------|--------|--------|--------|--------|--------|
| LSRII | 488 nm | 780/60 | 695/40 | 670/14 | 610/20 | 576/26 | 530/30 | 488/10 |
| | 633 nm | 780/60 | 730/45 | 660/20 | | | | |
| | 405 nm | 610/20 | 525/50 | 440/40 | | | | |
| | 355 nm | 530/30 | 440/40 | | | | | |
| Cytotflex S | 488 nm | 690/50 | 525/40 | 488/8 | | | | |
| | 561 nm | 780/60 | 690/50 | 610/20 | 585/42 | | | |
| | 633 nm | 780/60 | 712/25 | 660/20 | | | | |
| | 405 nm | 660/20 | 610/20 | 525/40 | 450/45 | | | |

| Instrument | Parameter | Acquisition seq 1 | Acquisition seq 2 |
|-------------------------|--|--------------------------|--------------------------|
| Leica TCS-SP8 | Pinhole | 67.9 μ m | 67.9 μ m |
| | PinholeAiry | 1 AU | 1 AU |
| | EmissionWavelength for PinholeAiry Calculation | 580 nm | 580 nm |
| | Excitation Beam Splitter | TD 488/552/638 | TD 488/552/638 |
| Hybrid Detectors | HyD 1 (nm) | | 410 - 460 |
| | HyD 2 (nm) | 492 - 522 | 560 - 571 |
| | HyD 3 (nm) | | 613 - 630 |
| | HyD 4 (nm) | 530 - 548 | 705 - 740 |
| | HyD 5 (nm) | 645 - 675 | |
| Solid state lasers (nm) | 405, Intensity (%): | - | 0.30 |
| | 488, Intensity (%): | 0.30 | - |
| | 552, Intensity (%): | - | 0.40 |
| | 638, Intensity (%): | 0.30 | 0.04 |

788